J. Mech. Phys. Solids 210 (2026) 106529

Contents lists available at ScienceDirect

Journal of the Mechanics and Physics of Solids

journal homepage: www.elsevier.com/locate/jmps

Spontaneous oscillations in eukaryotic cilia and photo-responsive rods

Daniele Agostinelli [a,1], Irene Anello [b,1], Reza Norouzikudiani [c,1], Antonio DeSimone [b,c,*]

[a] DIISM, UNIVPM, Via Brecce Bianche, 12, Ancona, 60131, Italy
[b] MathLab, SISSA, Via Bonomea, 265, Trieste, 34136, Italy
[c] The Biorobotics Institute, Scuola Superiore Sant'Anna, V.le R. Piaggio 34, Pontedera, 56025, Italy

ARTICLE INFO

Keywords:
Hopf bifurcation
Self-oscillations
Liquid crystal elastomers
Eukaryotic cilia
Active matter
Nonlinear dynamics
Chemomechanics

ABSTRACT

We present a comparative analysis of the chemo-mechanical mechanisms that drive spontaneous oscillations in two distinct active filamentous structures: photo-chemically deformable liquid crystal elastomer (LCE) rods and ATP-powered eukaryotic cilia. Using a unified framework of active planar rods, we develop simplified mathematical models for both systems. We reduce the governing partial differential equations to one-degree-of-freedom (1-DOF) nonlinear oscillators, each undergoing a supercritical Hopf bifurcation. For these reduced models, we obtain explicit analytical expressions for the onset and characteristics of self-sustained oscillations. Despite the common mathematical structure, the underlying physical mechanisms are fundamentally different. For LCEs, self-oscillation is an inertial phenomenon driven by an elastic-inertial feedback over the timescale of the photochemical reaction. In contrast, cilia live in the inertia-less regime, and the instability is driven by a negative effective damping (motive force) that arises from the mechanochemistry of molecular motors. The analytical predictions for critical activation thresholds, frequencies, and amplitudes agree with full nonlinear simulations, providing quantitative insight into the dynamics of these complex self-oscillating systems.

1. Introduction

Understanding the mechanisms by which microorganisms convert energy, from external sources distributed in the environment, into useful mechanical work for locomotion and transport in a fluid may provide new insight into biology and new concepts for bioinspired devices. Spontaneous oscillations of eukaryotic cilia (also called eukaryotic flagella, especially with reference to unicellular flagellate organisms), powered biochemically by ATP hydrolysis, are at the root of many important biological functions (Alberts et al., 2022). Inspired by these important natural templates, artificial motile systems - driven by a variety of mechanisms such as muscle cells, electromagnetic fields, light, or self-diffusiophoresis (see, e.g., Gompper et al., 2020 and the references cited therein for some concrete examples) - are being considered for applications in energy harvesting, microfluidics, and targeted drug delivery.

In this paper, we analyze and compare two active elastic filamentous structures that undergo oscillatory instabilities: photo-deformable liquid crystal elastomer (LCE) rods, which display self-oscillatory behaviour under uniform illumination, and eukaryotic cilia (Alberts et al., 2022), whose beating is powered by internal molecular motors. Although the physical mechanisms responsible

* Corresponding author.
E-mail address: desimone@sissa.it, a.desimone@santannapisa.it (A. DeSimone).
[1] These authors have contributed equally to this work.

https://doi.org/10.1016/j.jmps.2026.106529
Received 1 October 2025; Received in revised form 20 December 2025; Accepted 23 January 2026
Available online 27 January 2026

for the activation are very different, both systems undergo a Hopf-type instability, where self-sustained oscillations emerge from a steady equilibrium state as a result of chemo-mechanical feedback. By simplifying the mathematical description of each problem, we aim to extract analytical insight into the underlying mechanisms and key quantitative information (such as the critical value of the activation source, amplitude, and frequency of beating, and the way in which they depend on the parameters of the system). We selected these two systems as case studies of spontaneous oscillations because they have attracted much attention in the recent literature and they represent complementary examples of distinct physical regimes of active filaments: eukaryotic cilia operate in a microscopic, inertia-less regime dominated by viscous drag, whereas LCE rods operate in a macroscopic inertial regime. By studying them together, we aim to highlight commonalities and differences between two benchmark examples of self-oscillating systems of great contemporary interest, which have often been compared on a purely qualitative basis. Our quantitative analysis allows us to export knowledge and insight from one to the other.

Ciliary beating plays a fundamental role in key biological processes, including locomotion (e.g., sperm cells and unicellular organisms) (Satir and Christensen, 2007) and mucociliary clearance in the respiratory system (Button et al., 2012). These oscillatory motions are generated by the axoneme, the cytoskeleton of eukaryotic cilia (Alberts et al., 2022). The architecture of the axoneme is highly conserved across species and is composed of nine microtubule doublets arranged in a cylindrical configuration, and connected by molecular motors. The axoneme functions as an active structure: the motors convert chemical energy (ATP) into mechanical work, by generating sliding forces between adjacent microtubules. These forces are transformed into bending waves by passive structural elements (both internal, such as nexins and cross-links, and external, such as the surrounding fluid). The system is often modelled as two elastic filaments subject to active internal forces, which drive a Hopf-type bifurcation (Brokaw, 1971; Lindemann, 1994; Camalet and Jülicher, 2000; Riedel-Kruse et al., 2007; Sartori et al., 2016; Oriola et al., 2017; Howard et al., 2022; Alouges et al., 2024; Anello et al., 2025), and we follow a similar approach. Many alternative models have been proposed in the vast available literature (Bayly and Wilson, 2015; Namdeo and Onck, 2016; Gallagher et al., 2023; Woodhams, 2025), also exploiting analogies with classical flutter instabilities of elastic rods under non-conservative loads (Clarke et al., 2024). The ciliary case introduces additional subtleties, including spatially distributed activity, negligible inertia, and the coexistence of multiple oscillatory modes. Oscillatory instabilities also occur in other biological systems, such as plant shoots, where delayed responses to environmental stimuli result in spontaneous motion (Lega and Goriely, 1999; Moulton et al., 2020; Agostinelli et al., 2020, 2021a,b). This recurrence of delay-driven oscillations highlights the broader interest of the mechanisms explored in this study.

Materials such as LCEs that morph in response to external stimuli are attracting growing interest. In particular, LCE rods can exhibit spontaneous oscillations under steady illumination (White et al., 2008; Zeng et al., 2019; Deng et al., 2024; Norouzikudiani et al., 2024). These photo-deformable systems are particularly relevant for emerging applications in soft robotics, autonomous actuators, microfluidics and energy-harvesting devices. In the case of interest here, namely, photochemically deformable rods, oscillatory behavior arises from delayed feedback that involves light absorption, chemical transformation of azo molecules, and mechanical deformation. Such delays may lead to overshooting of the mechanical equilibrium and to periodic motion via a Hopf-type bifurcation. Compared to the biological case of ATP-powered ciliary beating, the driving mechanism is due to external stimuli rather than to internal molecular motors. The dynamics are shaped by photochemical time lags and nonlocal coupling effects, for instance due to self-shadowing along the rod.

Despite their differences, there exist regimes in which both photochemically deformable LCE rods and ATP-powered eukaryotic cilia can be described well by one-degree-of-freedom nonlinear oscillator models sharing the same structure, see Eqs. (23) and (40), and the same linearization, given by

$$a_{\text{eff}}\dddot{q}(t) + m_{\text{eff}}\ddot{q}(t) + d_{\text{eff}}\dot{q}(t) + k_{\text{eff}}q(t) = 0\,. \tag{1}$$

Here q is a scalar parameter that quantifies the amplitude of the oscillations, and the coefficients represent the effective jerk, inertia, damping and elastic properties. The oscillators (23) and (40) exhibit a supercritical Hopf bifurcation: formulas for the amplitude and frequency of oscillations, and for critical values of the activation parameter are derived in Sections 3 and 4, clarifying their dependence on the effective parameters a_{eff}, m_{eff}, d_{eff}, k_{eff} in a completely explicit manner. These effective parameters arise from different physical mechanisms in the two systems: for example, the effective inertia m_{eff} is nonzero for both systems, but the physical inertia is negligible in the case of eukaryotic cilia, while it is nonzero, and essential for self-oscillations, in the case of LCEs. The common structure of Eq. (1) explains why the two systems exhibit similar oscillatory phenomena. The dependence of the effective parameters on different physical mechanisms explains in which sense the two systems are different, how the oscillations they exhibit depend on different physical parameters, and how they can be controlled.

The paper is organized as follows. In Section 2, we briefly review the mechanics of planar (two-dimensional) active elastic rods, which is the common framework used to describe both systems. Section 3 is focused on the photo-deformable beam model. We first present the full model and its reduction to a one-degree-of-freedom nonlinear model, then we analyze light-powered oscillations in both models, and finally compare the results. Section 4 is devoted to ATP-driven cilia, following the same structure as for the photo-deformable beams. Section 5 presents the main conclusions of the comparative analysis of the two systems.

2. Mechanics of active planar rods

In this section, we introduce the mechanics of active planar inextensible rods lying on the plane spanned by $\mathbf{e}_1$ and $\mathbf{e}_2$, which will serve as a general framework for the modeling of photo-deformable LCE beams and ATP-driven cilia.

At each time t, $\mathbf{r}(s,t)$ denotes the centerline of the (inextensible) rod, parametrized by the arc-length coordinate $s \in [0, L]$. In the following, a prime ($'$) denotes differentiation with respect to the arc-length s, and a superimposed dot ($\dot{}$) with respect to time t. We denote by $\theta(s,t)$ the angle between the unit tangent vector $\mathbf{t}(s,t)$ and the horizontal direction such that

$$\mathbf{t}(s,t) = \mathbf{r}'(s,t) = \cos(\theta(s,t))\mathbf{e}_1 + \sin(\theta(s,t))\mathbf{e}_2. \tag{2}$$

The following force- and moment-balance equations hold

$$\begin{cases} M'(s,t) + (\mathbf{t}(s,t) \times \mathbf{R}(s,t)) \cdot \mathbf{e}_3 + m(s,t) = 0, \\ \mathbf{R}'(s,t) + \mathbf{g}(s,t) = 0, \end{cases} \tag{3}$$

where $M(s,t)$ and $\mathbf{R}(s,t)$ are the internal moment and force, respectively, $m(s,t)$ is the density of active and external moments, $\mathbf{g}(s,t) = \mathbf{g}(\dot{\mathbf{r}}(s,t), \ddot{\mathbf{r}}(s,t))$ is the density of the external force, which will be specified depending on the context. Throughout this paper, we consider clamped-free boundary conditions

$$\theta(0,t) = 0, \quad \dot{\mathbf{r}}(0,t) = \mathbf{0}, \quad \mathbf{R}(L,t) = \mathbf{0}, \quad M(L,t) = 0, \tag{4}$$

at all times t. The last condition expresses the fact that no external couple is applied at the free end $s = L$.
For the constitutive response to bending, we assume the linear law

$$M = B\big(\kappa - \kappa_0\big), \tag{5}$$

where B is the bending stiffness, $\kappa = \theta'$ is the rod curvature, and $\kappa_0 = \theta_0'$ is the spontaneous (active) curvature.
By integrating the second equation in (3), we can write the shear force as

$$T(s,t) := (\mathbf{t}(s,t) \times \mathbf{R}(s,t)) \cdot \mathbf{e}_3 = \left(\int_s^L \mathbf{g}(\sigma,t)\, d\sigma \right) \cdot \mathbf{n}(s,t), \tag{6}$$

where $\mathbf{n} = \big(-t_2, t_1, 0\big)$ is normal to the tangent vector $\mathbf{t} = \big(t_1, t_2, 0\big)$. Then we can solve Eq. (3) for the tangent angle θ after imposing boundary conditions (4).

In the following, we consider (active) systems where either m or κ_0 is not known a priori but is governed by evolution laws that quantify the response of the system to incoming energy flux from the environment, which is either light or ATP.

3. Photo-deformable beams

3.1. Mathematical model

We model a photo-chemically deformable azo-based liquid crystal elastomer (LCE) beam as a planar inextensible rod with a rectangular cross section of thickness h (length in the direction $\mathbf{n}$, normal to the tangent) and width w (length in the direction $\mathbf{e}_3$). As in Norouzikudiani et al. (2023), we prescribe in Eq. (3) the external moment and force as follows. The external moment accounts for the rotary inertia, i. e.,

$$m = -\rho I \ddot{\theta}, \tag{7}$$

where ρ is the mass density, $I = wh^3/12$ is the second moment of area of the cross-section corresponding to the direction $\mathbf{n}$. The external force includes viscous drag and translational inertia, $\mathbf{g} = -\boldsymbol{\Xi}\dot{\mathbf{r}} - \rho A \ddot{\mathbf{r}}$, where $A = wh$ is the cross-sectional area, and $\boldsymbol{\Xi} := \xi_n\, \mathbf{n} \otimes \mathbf{n} + \xi_t\, \mathbf{t} \otimes \mathbf{t}$ is the friction tensor with the normal and tangential friction coefficients, ξ_n and ξ_t. For simplicity, we assume isotropic friction with $D := \xi_n = \xi_t$, so that $\boldsymbol{\Xi} = D\mathbf{I}$ and the external force reduces to

$$\mathbf{g} = -D\dot{\mathbf{r}} - \rho A \ddot{\mathbf{r}}. \tag{8}$$

Finally, the bending stiffness in the constitutive Eq. (5) is given by $B = EI$, where E is the Young's modulus of the material.

As shown in Fig. 1, the beam is clamped at its left end and subjected to a uniform constant light intensity $\bar{J}$ that shines horizontally from the right. The material is initially in the nematic phase, with nematic director $\bar{\mathbf{n}}$. At the microscopic level, light absorption induces the isomerization of trans molecules into cis molecules, lowering the nematic order of the liquid crystal molecules. This process causes a macroscopic contraction of the material in the nematic direction $\bar{\mathbf{n}}$. When light is absorbed nonuniformly across the thickness, e.g., if only one side of the beam is exposed, the resulting strain gradient leads to bending. Neglecting thermal effects and assuming small fractions of cis-molecules, we model the macroscopic response of the beam to light by prescribing the time evolution of the spontaneous curvature κ_0 as

$$\dot{\kappa_0} = -\frac{\kappa_0}{\tau} - \lambda \bar{J} \sin\theta, \tag{9}$$

where τ is the characteristic relaxation time set by the average cis-lifetime, and λ is a positive proportionality constant. In particular, $\lambda = 12c\Gamma\beta/h^3$ where c is the proportionality coefficient between the spontaneous strain and the fraction of cis-molecules, Γ is the material absorption constant, and $\beta = -d(d - h/2 - \exp(-h/d)(d + h/2)) > 0$ is a parameter determined by the light penetration depth d and the beam thickness h. In Appendices A.1 and A.2, we derive Eq. (9) from a more general model (Norouzikudiani et al., 2023), under the assumption of low fractions of cis-molecules, which also allows us to consider the rod as inextensible. The applicability of such an approximation is supported by numerical simulations discussed in Appendix A.3.2.

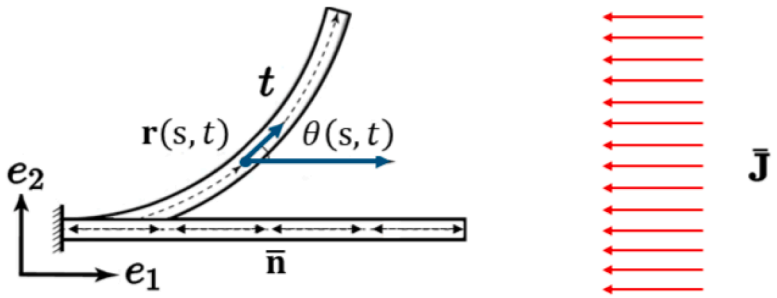

Fig. 1. Schematic of an LCE beam clamped at the left end and illuminated by a uniform light intensity $\bar{J}$. The beam centerline is described by the position $\mathbf{r}(s,t)$ and the tangent vector $\mathbf{t}(s,t)$ that forms the angle $\theta(s,t)$ with $\mathbf{e}_1$; $\bar{\mathbf{n}}$ denotes the nematic director, parallel to the tangent vector, and shown in the reference configuration.

The sinusoidal dependence on the tangent angle θ accounts for the local light absorption on the illuminated side of the beam, while we neglect non-local self-shadowing effects by which a part of the beam may project a shadow on other parts. Since this assumption is accurate for relatively short beams (see Appendix A.3.1), we restrict our study to beams of length $L \leq 20$ mm.

In summary, the system consists of Eqs. (3), (5), (7), (8), (9), and boundary conditions (4), i. e.,

$$\begin{cases} B\big(\theta''(s,t) - \kappa_0'(s,t)\big) + \mathbf{R}(s,t)\cdot\mathbf{n}(s,t) - \rho I\ddot{\theta}(s,t) = 0, \\ \mathbf{R}'(s,t) = D\dot{\mathbf{r}}(s,t) + \rho A\ddot{\mathbf{r}}(s,t), \\ \dot{\kappa_0}(s,t) = -\frac{1}{\tau}\kappa_0(s,t) - \lambda\bar{J}\sin\theta(s,t), \\ \theta(0,t) = 0, \quad \dot{\mathbf{r}}(0,t) = \mathbf{0}, \\ \mathbf{R}(L,t) = \mathbf{0}, \quad M(L,t) = 0. \end{cases} \tag{10}$$

3.1.1. Limit of small deformations

Integrating in space the second equation of (10), we get

$$B\big(\theta''(s,t) - \kappa_0'(s,t)\big) + \int_L^s (D\dot{\mathbf{r}} + \rho A\ddot{\mathbf{r}})\, d\sigma \cdot \mathbf{n}(s,t) - \rho I\ddot{\theta}(s,t) = 0. \tag{11}$$

In the limit of small deformations about the equilibrium $(\theta, \kappa_0) = (0,0)$, we can linearize and differentiate twice Eq. (11) to get the linear equation

$$B(\theta'''' - \kappa_0''') + D\dot{\theta} + \rho A\ddot{\theta} - \rho I\ddot{\theta}'' = 0. \tag{12}$$

Keeping the nonlinearity that arises from the dynamics of light illumination, we derive the following semilinear system

$$\begin{cases} B(\theta'''' - \kappa_0''') + D\dot{\theta} + \rho A\ddot{\theta} - \rho I\ddot{\theta}'' = 0, \\ \dot{\kappa_0} = -\frac{\kappa_0}{\tau} - \lambda\bar{J}\sin\theta, \\ \theta(0) = 0, \quad \theta'''(0) = {\kappa_0}''(0), \\ \theta''(L) = {\kappa_0}'(L), \quad \theta'(L) = \kappa_0(L). \end{cases} \tag{13}$$

The second boundary condition follows from $\dot{\mathbf{r}}(0,t) = 0$, implying $T'(0) = 0$ at first order. The third boundary condition is derived by neglecting the contribution of rotational inertia.

Linearizing also the evolution law for the spontaneous curvature about the equilibrium $(\theta, \kappa_0) = (0,0)$, we get the linear system

$$\begin{cases} B(\theta'''' - \kappa_0''') + D\dot{\theta} + \rho A\ddot{\theta} - \rho I\ddot{\theta}'' = 0, \\ \dot{\kappa_0} = -\frac{\kappa_0}{\tau} - \lambda\bar{J}\theta, \\ \theta(0) = 0, \quad \theta'''(0) = {\kappa_0}''(0), \\ \theta''(L) = {\kappa_0}'(L), \quad \theta'(L) = \kappa_0(L). \end{cases} \tag{14}$$

3.1.2. Model reduction to 1 DOF

In this section, we reduce (13) to a one-degree-of-freedom (1-DOF) model that is appropriate to investigate light-induced oscillations in the regime of small deformations. We capture the essential features of the dynamics of the system by the assumed mode procedure[1] (Meirovitch, 1997). In particular, we assume that

$$\theta(s,t) = \varphi(s)q(t), \quad \kappa_0(s,t) = \varphi'(s)q_0(t), \tag{15}$$

[1] The assumed mode procedure is a special case of the Galerkin method, in which the trial functions are chosen as the mode shapes of the associated undamped, unforced linear system. This choice ensures exact satisfaction of the geometric boundary conditions and generally yields rapid convergence of the modal expansion.

where φ is the first mode of the undamped Euler-Bernoulli beam with clamped-free boundary conditions, i. e.,

$$\begin{cases} B\varphi''''(s) - b_1^4\varphi(s) = 0, \\ \varphi(0) = \varphi'''(0) = 0, \\ \varphi'(L) = \varphi''(L) = 0, \end{cases} \qquad \text{with } b_1 \approx \frac{0.596864\pi}{L}. \tag{16}$$

More explicitly, we consider the mode

$$\varphi(s) = \left(\frac{-\sin b_1 L + \sinh b_1 L}{\cos b_1 L + \cosh b_1 L}\right)\left(-\cosh b_1\ s + \cos b_1\ s\right) + \left(\sinh b_1\ s + \sin b_1\ s\right), \tag{17}$$

corresponding to the first natural angular frequency

$$\omega_1 := b_1^2\sqrt{\frac{B}{\rho A}}. \tag{18}$$

By substituting the assumed forms (15) into (13) and using the Taylor expansion $\sin(\theta) \sim \theta - \theta^3/6$, we arrive at

$$\begin{cases} \left[Bb_1^4\left(q(t) - q_0(t)\right) + D\dot{q}(t) + \rho A\ddot{q}(t)\right]\varphi(s) - \rho I\ddot{q}\varphi''(s) = 0, \\ \varphi'(s)\dot{q}_0(t) = -\varphi'(s)\frac{q_0(t)}{\tau} - \lambda\bar{J}\varphi(s)q(t) + \frac{\lambda\bar{J}}{6}(\varphi(s)q(t))^3, \end{cases} \tag{19}$$

while all boundary conditions are implicitly satisfied. We obtain the reduced 1-DOF model by projecting the first equation on φ and the second equation on φ', namely,

$$\begin{cases} M\ddot{q}(t) + D\dot{q}(t) + K\left(q(t) - q_0(t)\right) = 0, \\ \dot{q}_0(t) = -\frac{1}{\tau}q_0(t) - \lambda\bar{J}\frac{c_2}{c_1}q(t) + \frac{\lambda\bar{J}}{6}\frac{c_3}{c_1}q(t)^3, \end{cases} \tag{20}$$

where

$$M = \rho\left(A + I\frac{c_1}{c_4}\right), \quad K = Bb_1^4, \tag{21}$$

$$c_1 = \int_0^L (\varphi')^2, \quad c_2 = \frac{\varphi^2(L)}{2}, \quad c_3 = \frac{\varphi^4(L)}{4}, \quad c_4 = \int_0^L \varphi^2, \tag{22}$$

which are all nonnegative constants. Notice that M, D and K are the inertia, viscosity and elasticity of the passive system (without light-induced activity), respectively.

By solving the first equation for q_0 and substituting it into the second equation, we can rewrite the system (20) as a single nonlinear "jerk" equation in $q(t)$, i. e.,

$$a_{\text{eff}}\dddot{q}(t) + m_{\text{eff}}\ddot{q}(t) + d_{\text{eff}}\dot{q}(t) + k_{\text{eff}}q(t) - \gamma_{\text{eff}}q(t)^3 = 0, \tag{23}$$

where $a_{\text{eff}} = \tau M$ is the effective jerk, $m_{\text{eff}} = \tau D + M$ is the effective inertia, $d_{\text{eff}} = \tau K + D$ is the effective damping, $k_{\text{eff}} = K\left(1 + \tau\lambda\bar{J}c_2/c_1\right)$ is the effective elasticity, and $\gamma_{\text{eff}} = \tau\lambda\bar{J}Kc_3/(6c_1)$ is the coefficient of the cubic stiffness, which acts as a softening since $\gamma_{\text{eff}} > 0$.

Eq. (23) is the equation of a nonlinear oscillator with equilibrium $q(t) \equiv 0$, and the linear terms have the following physical interpretation. Light absorption amplifies the elastic response of the system by the term $\tau\lambda\bar{J}c_2/c_1$; moreover, the cis-isomerization dynamics introduces a jerk effect through inertia and affects both the dissipative viscosity and the inertia of the system, by the elastic-related term τK and the viscous-related term τD, respectively. In Appendix B, we perform the stability analysis for a general model encompassing Eq. (23) as a special case.

3.2. Analysis of the light-powered oscillations

In this section, we analyze the dynamics of the models derived in Section 3.1 for LCE photo-deformable beams subjected to light illumination. We start by studying the 1-DOF model (20), which undergoes a supercritical Hopf bifurcation as the light intensity $\bar{J}$ exceeds a threshold, such that an initial perturbation of the equilibrium triggers sustained light-powered oscillations; for this reduced model, we obtain analytical expressions for the threshold light intensity for the onset of self-oscillations, and the oscillation frequency and amplitude near onset (Section 3.2.1). Similarly to the 1-DOF model, the full model (10) presents a Hopf-like bifurcation. First, we perform a linear stability analysis to identify the critical values of frequency and light intensity (Section 3.2.2). Then, we numerically solve the nonlinear model (10) to analyze the periodic solutions and we compare these results with those obtained through the reduced 1-DOF model (20) (Section 3.2.3). In the following, numerical simulations of the models are based on the parameters provided in Table 1.

Table 1
Summary of model parameters for the photo-deformable LCE beam (Norouzikudiani et al., 2024).

Parameter	Description	Value
E	Young's modulus	10^8 Pa
w	Beam width	10^{-3} m
h	Beam thickness	$50 \cdot 10^{-6}$ m
ρ	Mass density	1400 kg/m^3
D	Viscosity coefficient	0.001 N·s/m^2
c	Strain - cis-fraction coefficient	0.05
τ	Cis-lifetime	0.1 s
d	Light penetration depth	$5 \cdot 10^{-6}$ m
Γ	Absorption constant	10^{-3} m^2/J

3.2.1. Hopf bifurcation in the 1-DOF model

Using the results in Appendix B, we conclude that the equilibrium of Eq. (23) undergoes an instability that is triggered by the linear effective stiffness, k_{eff}. Indeed, for sufficiently high values of the light intensity $\bar{J}$, the jerk-modulated stiffness, $a_{\text{eff}}k_{\text{eff}}$, overcomes the inertia-modulated damping, $m_{\text{eff}}d_{\text{eff}}$, so that energy is injected at a higher rate than it is dissipated and the equilibrium loses stability. In the overdamped limit, where inertia is negligible ($\rho = 0$), the equilibrium is always stable because the effective jerk vanishes ($a_{\text{eff}} = \tau M = 0$) and the destabilizing condition $a_{\text{eff}}k_{\text{eff}} > m_{\text{eff}}d_{\text{eff}}$ is never fulfilled. In other terms, the instability is driven by an elastic-inertial feedback over the timescale τ, represented by the jerk coefficient a_{eff}. For any $\rho > 0$ (and hence $a_{\text{eff}} > 0$), the system undergoes a Hopf bifurcation once the light intensity $\bar{J}$ exceeds the critical value

$$\bar{J}_c = \frac{c_1 D}{c_2 \lambda K}\left[\frac{K}{M} + \frac{1}{\tau^2} + \frac{D}{\tau M}\right] \approx \frac{c_1 D}{c_2 \lambda B b_1^4}\left(\omega_1^2 + \frac{1}{\tau^2} + \frac{D}{\rho A \tau}\right), \tag{24}$$

which corresponds to the critical oscillation frequency

$$\omega_c = \sqrt{\frac{k_{\text{eff}}}{m_{\text{eff}}}} = \sqrt{\frac{d_{\text{eff}}}{a_{\text{eff}}}} = \sqrt{\frac{\tau K + D}{\tau M}} \approx \sqrt{\omega_1^2 + \frac{D}{\tau \rho A}}. \tag{25}$$

The approximations in Eqs. (24) and (25) follow observing that $I c_1/c_4 \sim A(h/L)^2 \ll A$, so that $M \approx \rho A$. Moreover, performing a scaling analysis with respect to the beam length L, we find that

$$\bar{J}_c \sim \frac{1}{L}, \quad \omega_c \sim \frac{1}{L^2}. \tag{26}$$

Eq. (25) states that the beating frequency of the system (20) is the first natural frequency of the undamped passive beam, ω_1, corrected by a term that depends on the cis lifetime τ and the ratio of damping to inertial forces. In summary, the active component of the beam determines the critical oscillation frequency.

Beyond the bifurcation point, the cubic term $-\gamma_{\text{eff}}q^3$ plays a crucial role. Indeed, having the opposite sign of $k_{\text{eff}}q$, it counteracts the linear instability by reducing the stiffness in the nonlinear regime. As a result, the Hopf bifurcation is supercritical, see Appendix B. At the critical light intensity $\bar{J}_c$, the equilibrium is destabilized and a stable limit cycle emerges. In particular, close to the bifurcation point, the beam dynamics converge to self-sustained oscillations with tip angle amplitude

$$R(\bar{J}) = 4\sqrt{1 - \frac{\bar{J}_c}{\bar{J}}}\ . \tag{27}$$

Finally, we numerically solve Eq. (23) using the `ode45` solver in MATLAB R2025a and the `NDSolve` function in Mathematica 14.0. The nonlinear simulations and the phase portraits confirm the occurrence of a supercritical Hopf bifurcation at the critical values of the light intensity $\bar{J}_c$ predicted analytically by Eq. (24), see Fig. 2. Moreover, close to the bifurcation point, the numerical results agree with the analytical expressions for the critical oscillation frequency (25) and the amplitude (27), see Fig. 7.

3.2.2. Linear stability analysis of the full linearized system

Having examined the reduced dynamics, we now return to the complete linear system (14) to perform the linear stability analysis. Assuming $\theta(s,t)$ and $\kappa_0(s,t)$ of the form $\theta(s,t) = \tilde{\theta}(s)e^{\sigma t}$ and $\kappa_0(s,t) = \tilde{\kappa}_0(s)e^{\sigma t}$, system (14) reduces to

$$\begin{cases} B(\tilde{\theta}'''' + \tilde{\kappa}_0''') + D\sigma\tilde{\theta} + \rho A\sigma^2\tilde{\theta} - \rho I\sigma^2\tilde{\theta}'' = 0, \\ \tilde{\kappa}_0 = -\chi\tilde{\theta}, \\ \tilde{\theta}(0) = \tilde{\theta}'''(0) + \chi\tilde{\theta}''(0) = 0, \\ \tilde{\theta}'(L) + \chi\tilde{\theta}(L) = \tilde{\theta}''(L) + \chi\tilde{\theta}'(L) = 0, \end{cases} \tag{28}$$

where $\chi = \chi(\bar{J}, \sigma) = \frac{\tau\lambda\bar{J}}{\tau\sigma+1}$.

We seek separable solutions of the form $\tilde{\theta}(s) = \sum_{j=1}^{4} A_j e^{\beta_j s}$, where β_j $(j = 1, \dots, 4)$ are distinct roots of the characteristic equation

$$B(\beta^4 + \chi\beta^3) - \rho I\sigma^2\beta^2 + D\sigma + \rho A\sigma^2 = 0. \tag{29}$$

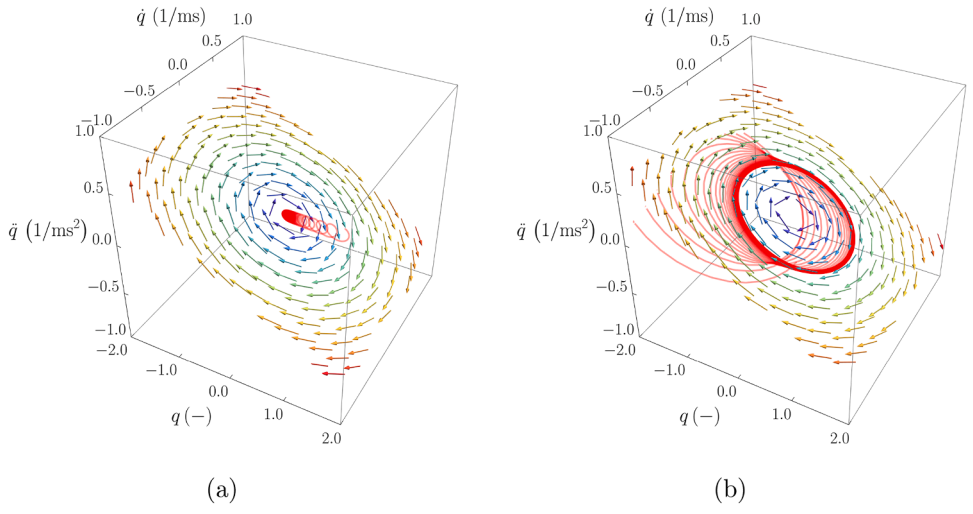

Fig. 2. Phase portraits of the 1-DOF model (20) for values of the light intensity $\bar{J}$ below (a) and above (b) the critical value $\bar{J}_c$. For visual clarity, the vector field $(q, \dot{q}, \ddot{q})$ is shown only on the 2D principal plane of the limit cycle. The red trajectory shows the dynamics of the solution associated with a perturbed initial condition. The transparency of the trajectory decreases with time. Model parameters are as in Table 1 and $L = 5$ mm. For such values, the critical light intensity is $\bar{J}_c \approx 19.4$ kW/m^2 and phase portraits are obtained for (a) $\bar{J} = 17.0$ kW/m^2 and (b) $\bar{J} = 22.0$ kW/m^2.

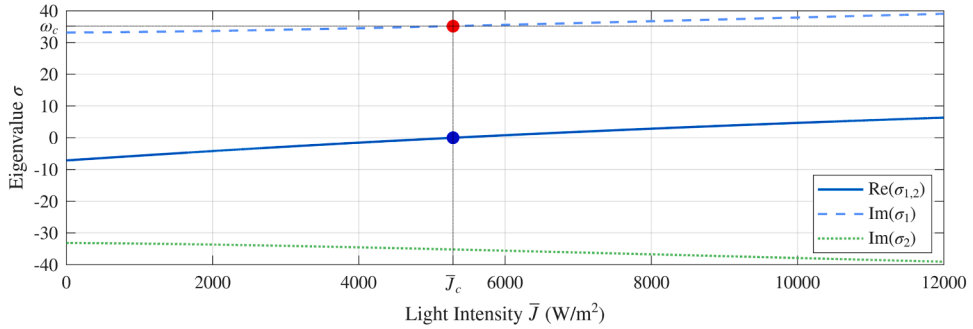

Fig. 3. Real (solid lines) and imaginary (dashed lines) part of the leading eigenvalue σ_1, and its complex conjugate eigenvalue σ_2, as functions of light intensity, for a beam of length $L = 20$ mm, and for the choice of parameters introduced in Table 1. We distinguish two regions corresponding to different dynamical responses for $\theta(s, t)$: damped oscillations for $\bar{J} < \bar{J}_c \approx 5289$ W/m^2 and oscillations with increasing amplitude for $\bar{J} > \bar{J}_c$.

The boundary conditions define a linear system $\mathbf{MA} = 0$, where

$$\mathbf{M} = \mathbf{M}(\chi(\bar{J}, \sigma)) = \begin{pmatrix} 1 & \dots & 1 \\ \beta_1^3 + \chi\beta_1^2 & \dots & \beta_4^3 + \chi\beta_4^2 \\ e^{\beta_1 L}(\beta_1^2 + \chi\beta_1) & \dots & e^{\beta_4 L}(\beta_4^2 + \chi\beta_4) \\ e^{\beta_1 L}(\beta_1 + \chi) & \dots & e^{\beta_4 L}(\beta_4 + \chi) \end{pmatrix} \tag{30}$$

and $\mathbf{A} = (A_1, A_2, A_3, A_4)^T$; to get a nonzero $\mathbf{A}$, and hence a nontrivial solution $\tilde{\theta}$, we prescribe $|\det \mathbf{M}(\bar{J}, \sigma)| = 0$.

As for the 1-DOF model, we find that there exists a critical light intensity $\bar{J}_c$ for which the real part of the leading eigenvalue σ_1 vanishes. The corresponding oscillation frequency is given by $\omega_c = \mathrm{Im}[\sigma_1(\bar{J}_c)]$. In particular, as the light intensity $\bar{J}$ exceeds the critical value $\bar{J}_c$, the real part of σ_1 passes from being negative to positive, indicating that the straight equilibrium undergoes an instability, see Fig. 3.

Fig. 4 shows the critical values $\bar{J}_c$ and ω_c as functions of the beam length, computed numerically as zeros of $\det \mathbf{M} = 0$, for the model parameters reported in Table 1. We find that the critical light intensity decreases monotonically as the beam length increases, indicating that longer LCE beams are inherently more susceptible to destabilization. We notice that these critical parameters are well approximated by the analytical formulas (24) and (25) obtained for the 1-DOF model (20). In particular, for the range of beam lengths shown in Fig. 4, the analytical expressions approximate the nonlinear critical values $\bar{J}_c$ and ω_c within a relative error of 12% and 3%, respectively.

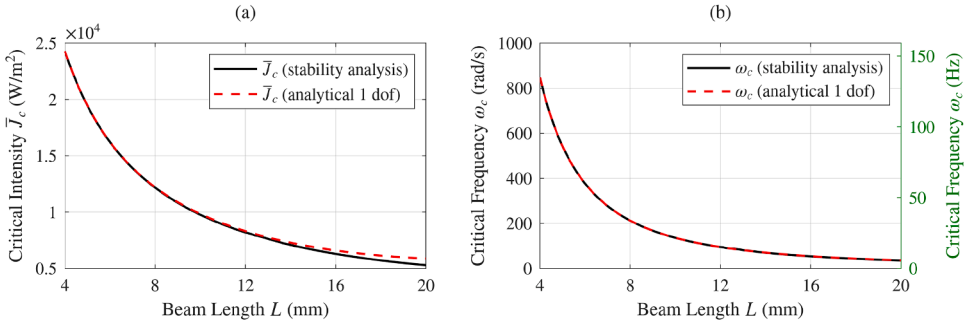

Fig. 4. Comparison of the critical intensity (a) and the critical frequency (b) for various beam lengths using the linear stability analysis of model (10) (solid lines) and the analytical expressions (24) and (25) for the 1-DOF model (20) (dashed lines), which follow the scaling $\bar{J}_c \sim 1/L$ and $\omega_c \sim 1/L^2$. Model parameters are as in Table 1.

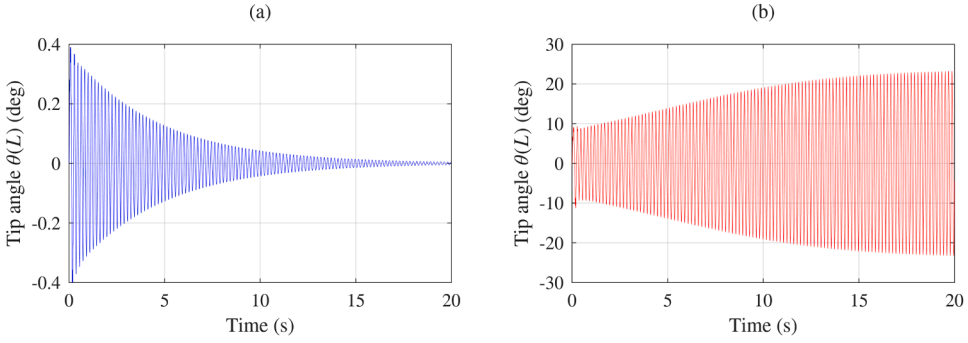

Fig. 5. Tip angle $\theta(L)$ obtained as numerical solution of (10) for a perturbed LCE beam of length $L = 20$ mm with light intensity $\bar{J} = 5100$ W/m^2 (a) and $\bar{J} = 5400$ W/m^2 (b). From the linear stability analysis, the critical light intensity is estimated as $\bar{J}_c \approx 5289$ W/m^2. Other model parameters are as in Table 1.

3.2.3. *Nonlinear simulations*

In this section, we explore the regime of large amplitude oscillations by solving numerically the nonlinear model in COMSOL Multiphysics (see Appendix C for more details on the numerical procedure). Material and geometric parameters are reported in Table 1.

Consistent with the linear stability analysis, we find that the trivial equilibrium becomes unstable as the light intensity exceeds the critical value $\bar{J}_c$. Moreover, in the unstable regime, small perturbations of the straight position are amplified and converge to a nontrivial time-periodic solution (a limit cycle). This behavior indicates a Hopf-like bifurcation at the critical light intensity $\bar{J}_c$ predicted by the linear stability analysis (see Figs. 5 and A.4 in Appendix A.3.2).

Finally, we compare the periodic solutions of the full model (10) with the reduced model (23), in terms of the beating frequency ω, the maximum tip angle $\theta(L)$, and the time evolution of the beam configurations. We show the results in Figs. 6 and 7 for LCE beams of length $L = 10$ mm and $L = 20$ mm, and other model parameters as in Table 1. The 1-DOF model (20) correctly captures the growth of the amplitude with increasing light intensity, highlighting the presence of a supercritical Hopf bifurcation (Wiggins, 2003). Below the critical parameter $\bar{J}_c$, oscillations are damped and the straight equilibrium is stable. Above the critical value, oscillations grow in amplitude until a stable limit cycle is reached. We conclude that the 1-DOF model captures the essence of the full model and provides good approximations for both the critical parameters and the overall beam dynamics, with lower accuracy for longer beams.

4. ATP-driven cilia

4.1. *Mathematical model*

We model the axonemal structure of a cilium as a planar system composed of two inextensible, elastic filaments of length L (representing microtubules) that are clamped at the base and free to slide relative to one another (Camalet and Jülicher, 2000; Riedel-Kruse et al., 2007; Sartori et al., 2016; Cass and Bloomfield-Gadêlha, 2023), see Fig. 8. The filaments are at a fixed distance $h \ll L$, and their position is given by

$$\mathbf{r}_{\pm}(s) = \mathbf{r}(s) \pm h\mathbf{n}(s)/2, \tag{31}$$

where $\mathbf{r}(s)$ is the neutral line curve, parametrized by the arc-length coordinate $s \in [0, L]$, and $\mathbf{n}(s)$ denotes the unit normal.

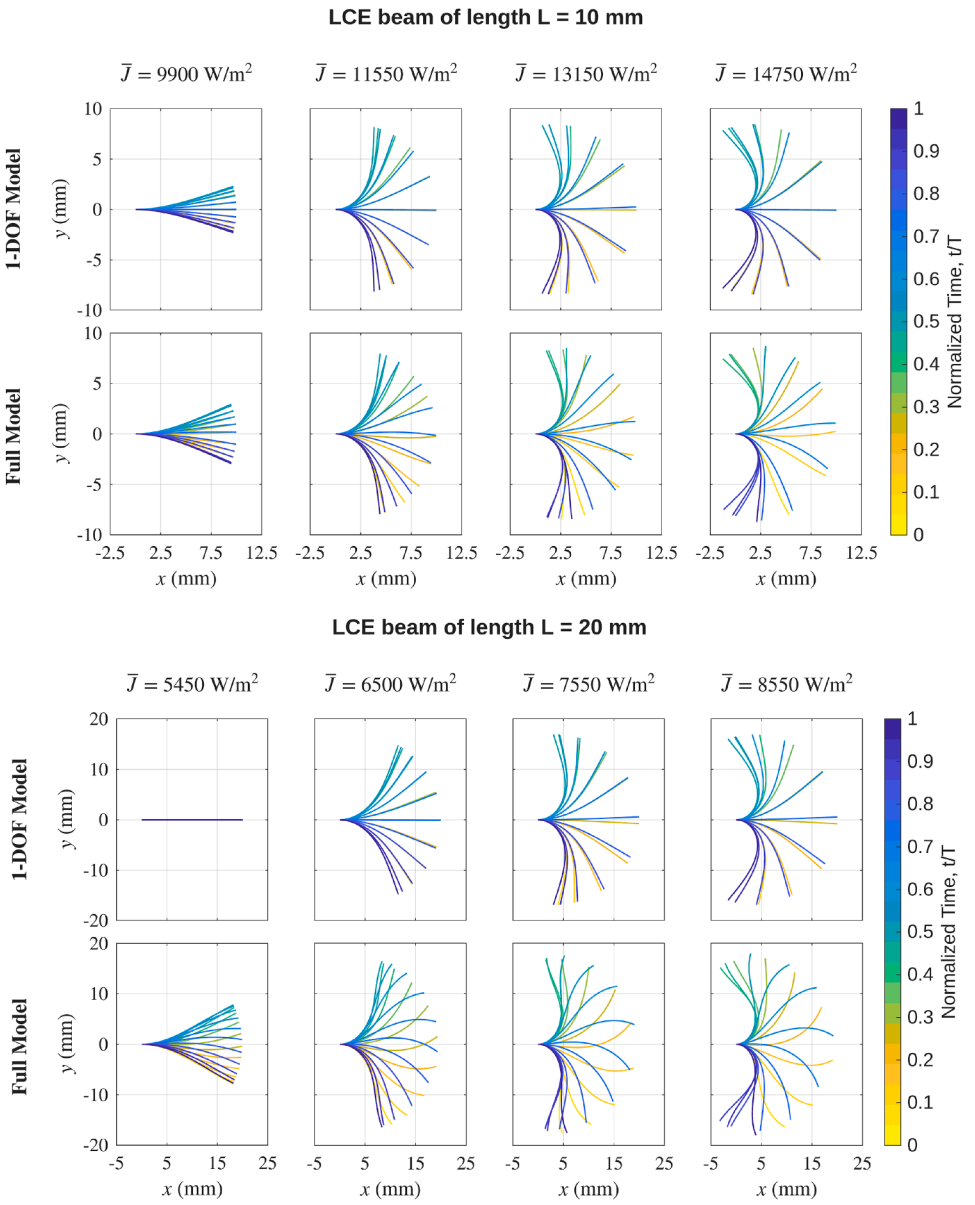

Fig. 6. Comparison of beam shapes between 1-DOF model (20) and full model (10) for different values of the light intensity $\bar{J}$, increasing from left to right. The beam length is (top) $L = 10$ mm and (bottom) $L = 20$ mm, while other model parameters are as in Table 1. Colors denote the normalized time t/T where T is the oscillation period.

Molecular motors are anchored to one filament and transiently bind to the other one, thus exerting forces in opposite directions. This mechanism creates a sliding displacement $u(s)$ between the filaments, which is defined as the difference between the accumulated arc-lengths along the two filaments up to $\mathbf{r}_+(s)$ and $\mathbf{r}_-(s)$, namely

$$u(s) = u(0) + \int_0^s (|\mathbf{r}'_-(\sigma)| - |\mathbf{r}'_+(\sigma)|)\, d\sigma = u(0) + h(\theta(s) - \theta(0)), \tag{32}$$

where $u(0)$ is the basal sliding (considered null for simplicity), and $\theta(s)$ is the tangent angle. The second equality in Eq. (32) follows by using Eq. (2) and assuming $|\theta'| < 2/h$. Differentiating Eq. (32) yields the kinematic relation between sliding and curvature

$$u' = h\theta'. \tag{33}$$

We model the neutral line of the cilium as a planar rod governed by Eqs. (3)–(5) with zero spontaneous curvature ($\kappa_0 = 0$), for which we need to specify the external force and moment densities. Since cilia are slender bodies in a low Reynolds number regime, we neglect any inertial term and adopt the resistive force theory (RFT, Gray and Hancock, 1955) approximation, expressing the external

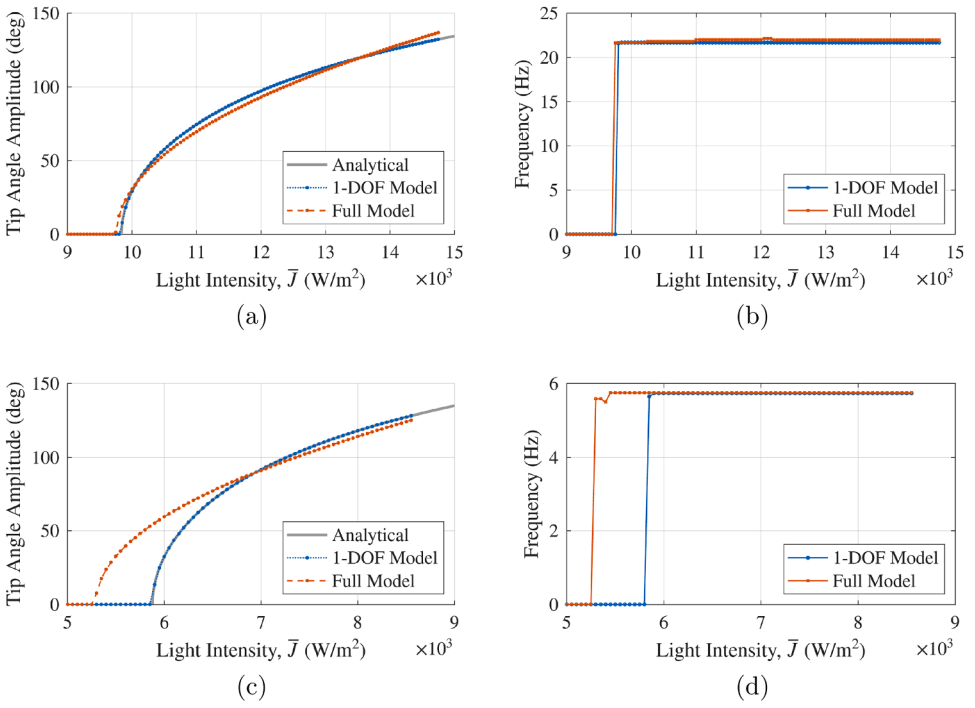

Fig. 7. Comparison between 1-DOF model (20) in blue and full model (10) in orange for (a,c) the maximum tip angle $\theta(L)$ and (b,d) the oscillation frequency ω by increasing the light intensity $\bar{I}$, near the bifurcation points. For the tip angle amplitude (a,c), numerical simulations are compared to analytical results, in gray, given by Eq. (27). The beam length is $L = 10$ mm (a,b) and $L = 20$ mm (c,d), while other model parameters are as in Table 1. Maximum tip angles and oscillation frequencies are extracted from periodic oscillations after the initial transient regime.

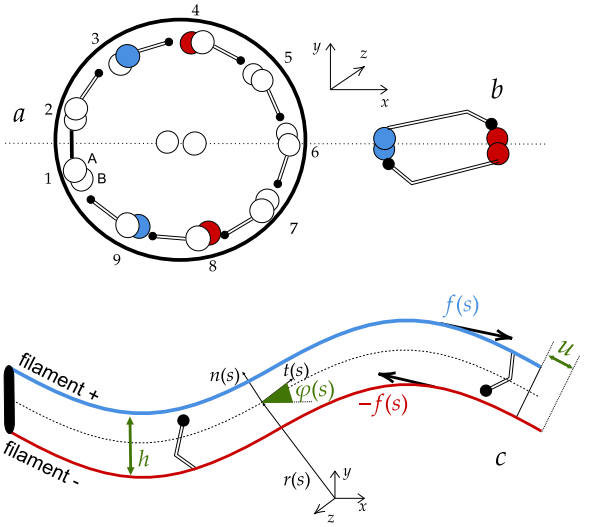

Fig. 8. From the axoneme to the two rows of molecular motors. (a) Cross-section of the axoneme when viewed from the base to tip, with numbering taken from Sartori et al. (2016). (b) Projection of the axoneme onto its bending plane. (c) The cilium is composed of two filaments fixed at the base.

drag force in Eq. (3) as

$$\mathbf{g} = -\boldsymbol{\Xi}\dot{\mathbf{r}}, \tag{34}$$

where $\boldsymbol{\Xi} := \xi_n \mathbf{n} \otimes \mathbf{n} + \xi_t \mathbf{t} \otimes \mathbf{t}$ is the friction tensor. In the RFT limit, the normal and tangential coefficients satisfy $\xi_n = 2\xi_t$. For the moment density, we write it as $m = hf$, where $f = f(s,t)$ is a force density acting at position s and at time t and it is the sum of two terms, $f = f_p + f_a$. The first term is the passive component of the motor force $f_p = -ku - \eta\dot{u}$, which resists sliding through elastic and viscous elements, represented by the constants $k > 0$ and $\eta > 0$, respectively. The second term is the active motor force resulting from

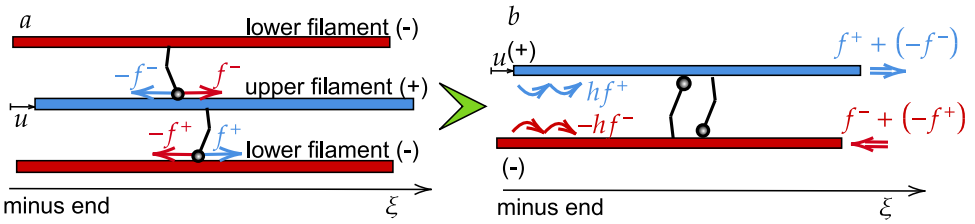

Fig. 9. (a) Unfolding of the cilium's two-filament structure from Fig. 8. The red filaments indicate the same structure, identified as the lower filament (-). This is shown again in (b). Antagonistic molecular motors exert a net force $f_a = f^+ - f^-$ on the upper filament, and the opposite force on the lower filament.

the antagonistic activity of molecular motors, i. e., $f_a = f^+ - f^-$, where f^+ and f^- are respectively the forces exerted on the upper and lower filament by the motors anchored to it while transiently binding to the other filament (see Fig. 9). A detailed theoretical framework describing these motor-filament interactions, known as the *sliding feedback model*, can be found in Jülicher and Prost (1995), Jülicher (1999), Alouges et al. (2024), Anello et al. (2025). This model captures how coordinated motor activity induces filament sliding to generate bending, while the resulting bending, in turn, modulates the chemical activity of the motors. In the present study, we adopt a simplified version of this framework: the *cubic model* introduced in Anello et al. (2025). In this formulation, the active force density f_a is related to the sliding velocity $\dot{u}$ through a nonlinear cubic law, which shows the essential feedback mechanisms in a reduced form, that is,

$$\dot{f}_a = -\frac{1}{\tau}\left(f_a - \lambda\dot{u} + \mu\tau\dot{u}^3\right). \tag{35}$$

Here, the destabilizing term $\lambda\dot{u}$ is modulated by a coefficient $\lambda > 0$ proportional to the ATP concentration, and the cubic term $-\mu\dot{u}^3$, $\mu > 0$, stabilizes the oscillations when $\dot{u}$ grows. The constant τ is the characteristic time for the binding/unbinding reaction of the molecular motors. Eq. (35) is to be thought of as the coarse-grained normal form coming from the micro-chemical system of equations that involve the probabilities of binding and unbinding of a collection of molecular motors (Jülicher et al., 1997).

In conclusion, recalling that $u = h\theta$ and that $m = hf = h(-kh\theta - \eta h\dot{\theta} + f_a)$, the nonlinear system for the cilia reads

$$\begin{cases} B\theta'' + \mathbf{R}(s,t)\cdot\mathbf{n}(s,t) + h(-kh\theta - \eta h\dot{\theta} + f_a) = 0, \\ \mathbf{R}'(s,t) = \xi_n \dot{r}_n \mathbf{n} + \xi_t \dot{r}_t \mathbf{t}, \\ \dot{f}_a = -\frac{1}{\tau}\left(f_a - \lambda h\dot{\theta} + \mu\tau h^3\dot{\theta}^3\right), \\ \theta(0,t) = 0, \quad \dot{\mathbf{r}}(0,t) = \mathbf{0}, \\ \mathbf{R}(L,t) = \mathbf{0}, \quad \theta'(L,t) = 0. \end{cases} \tag{36}$$

4.1.1. Limit of small deformations

As for the photo-deformable LCE beams (Eq. (13) in Section 3.1.1), we derive the semilinear system where the beam equation is written in the limit of small deformations around $(\theta, f_a) = (0,0)$, but we keep the nonlinearity given by the active term f_a. Therefore, the semilinear system for the cilia is

$$\begin{cases} B\theta'''' + \xi_n\dot{\theta} + h(-kh\theta - \eta h\dot{\theta} + f_a)'' = 0, \\ \dot{f}_a = -\frac{1}{\tau}\left(f_a - \lambda h\dot{\theta} + \mu\tau h^3\dot{\theta}^3\right), \\ \theta(0) = 0, \quad B\theta'''(0) + hf'(0) = 0, \\ \theta'(L) = 0, \quad B\theta''(L) + hf(L) = 0, \end{cases} \tag{37}$$

and the linearized version is

$$\begin{cases} B\theta'''' + \xi_n\dot{\theta} + h(-kh\theta - \eta h\dot{\theta} + f_a)'' = 0, \\ \dot{f}_a = -\frac{1}{\tau}\left(f_a - \lambda h\dot{\theta}\right), \\ \theta(0) = 0, \quad B\theta'''(0) + hf'(0) = 0, \\ \theta'(L) = 0, \quad B\theta''(L) + hf(L) = 0. \end{cases} \tag{38}$$

4.1.2. Model reduction to 1 DOF

As for the photo-deformable LCE beams (Section 3.1.2), we reduce the semilinear system (37) to a one-degree-of-freedom (1-DOF) model that captures the key features of the system. We adopt the assumed mode procedure (Meirovitch, 1997) and set

$$\theta(s,t) = \varphi(s)q(t), \quad f(s,t) = \varphi''(s)q_0(t), \tag{39}$$

where $f = f_a - kh\theta - \eta h\dot{\theta}$ and φ is the first mode of the undamped Euler-Bernoulli beam with clamped-free boundary conditions, already introduced in Section 3.1.2 and given by Eq. (17). Analogously to the LCE model, we substitute the ansatz (39) into Eq. (37), and project the resulting equations onto φ, obtaining a single nonlinear equation for $q(t)$,

$$m_{\text{eff}}\ddot{q}(t) + d_{\text{eff}}\dot{q}(t) + k_{\text{eff}}q(t) + \gamma_{\text{eff}}\dot{q}(t)^3 = 0, \tag{40}$$

Table 2
Characteristic parameters of the flagella of *Chlamydomonas*.

Parameter	Definition	Values
B	Bending rigidity	400 pN μm^2
h	Inter-filament distance	0.06 μm
ξ_n	Normal fluid viscosity (RFT)	0.0034 pN $\cdot$ s/μm^2
k	Internal elasticity	$15 \cdot 10^3$ pN/μm^2
η	Internal viscosity	0.1 pN $\cdot$ s/μm^2
τ	Characteristic motor switching time	0.0038 s
μ	Coefficient of cubic term	20 pN $\cdot$ s^2/μm^4

Table 3
Comparison of the instability mechanisms in photo-responsive LCE rods and ATP-driven cilia. Although the two systems have similar oscillator equation, the physical origin of the instability and the role of activity are fundamentally different.

Feature	Photo-responsive LCEs	ATP-driven cilia
Physical regime	Inertial (Non-negligible Reynolds)	Overdamped / Inertia-less (Low Reynolds)
Feedback variable	Position (θ) $\dot{\kappa}_0 = -\frac{\kappa_0}{\tau} - \lambda \bar{J} \sin\theta$	Velocity ($\dot{\theta}$) $\dot{f}_a = -\frac{f_a}{\tau} + \frac{\lambda h \dot{\theta}}{\tau} - \mu h^3 \dot{\theta}^3$
ODE structure	3$^{\text{rd}}$ order ($a \neq 0$) $a\dddot{q} + m\ddot{q} + d\dot{q} + kq - \gamma q^3 = 0$	2$^{\text{nd}}$ order ($a = 0$) $m\ddot{q} + d\dot{q} + kq + \gamma q^3 = 0$
Instability driver	Elastic-inertial coupling	Negative effective damping
Role of activity	Light intensity $\bar{J}$ modifies *effective stiffness* via time-delayed curvature	ATP concentration λ modifies *effective damping* via motor kinetics
Critical frequency	Inertial-elastic balance $\omega_c^2 = \frac{K + D/\tau}{M}$	Viscous-elastic balance $\omega_c^2 = \frac{K}{D\tau}$

where $m_{\text{eff}} = \tau D$ is the effective inertia, $d_{\text{eff}} = \tau K + D - \lambda$ is the effective damping, $k_{\text{eff}} = K$ is the effective elasticity, and $\gamma_{\text{eff}} = \tau \mu c_3 h^2 / c_2$ is the coefficient of the cubic damping, which is dissipative since $\gamma_{\text{eff}} > 0$. D and K denote the effective damping and elasticity of the passive system (without ATP-powered activity),

$$D = \eta + \frac{c_1}{c_2 h^2 b_1^4} \xi_n \qquad \text{and} \qquad K = k + \frac{c_1}{c_2 h^2 b_1^4} B b_1^4, \tag{41}$$

with the projection constants

$$c_1 = -\int_0^L \varphi'' \varphi = \int_0^L (\varphi')^2 > 0, \; c_2 = \int_0^L \varphi^2 > 0, \; c_3 = \int_0^L \varphi^4 > 0. \tag{42}$$

Eq. (40) describes a nonlinear oscillator with equilibrium $q(t) \equiv 0$. Although the passive system has no inertia, active forces introduce an effective mass τD, related to the internal and external viscosities. The chemical activity also contributes to the effective damping by a term related to the ATP concentration, λ, and another term associated with the elastic properties of the system, τK.

In contrast to the LCE case, Eq. (40) is a second-order equation with no jerk term, due to the lack of inertia in the passive system. We perform the stability analysis of this model in Appendix B.

4.2. Analysis of the ATP-driven oscillations

When the ATP concentration is low, the net active force f_a is zero, the motors are stalled, and the straight filament remains in a stable equilibrium. Although each motor still exerts a nonzero force on the filament to which it is attached, these forces balance out, resulting in no net active force. This creates a tug-of-war scenario between the two systems of antagonistic motors, and ATP acts as a bifurcation parameter. When the ATP concentration exceeds a critical threshold, the system undergoes a Hopf-like bifurcation, and the motor-filament dynamics transitions from a stationary state to one of sustained oscillations. Analogously to the case of light-powered oscillations for LCE beams (Section 3.2), we start by studying the 1-DOF model (Section 4.2.1) and then, after performing a linear stability analysis (Section 4.2.2), we numerically solve the full model and compare it with the reduced one (Section 4.2.3).

In the following, when presenting results for varying cilia lengths, we use the dimensionless sperm number, which quantifies the ratio between viscous and bending forces in the system, i. e.,

$$S_p = \frac{L}{L_0}, \qquad L_0 = \left(\frac{\tau B}{\xi_n} \right)^{1/4} \tag{43}$$

where L_0 is a characteristic length that was introduced by Machin (1958). Similarly to the photo-deformable LCE beams, we restrict our analysis to the regime of relatively high L_0, i. e., the viscous forces are negligible with respect to the elastic ones, and the sperm number $S_p \leq 2$. In this regime, cilia are relatively short ($L \leq 2L_0$) and the first mode used in the reduced 1-DOF model can provide a good approximation to the full model. We consider *Chlamydomonas* as a case study of such "short" cilia, with the relevant model parameters provided in Table 2, for which the characteristic length is $L_0 \approx 4.6$ μm.

4.2.1. Hopf bifurcation in the 1-DOF model

Using the results in Appendix B, we conclude that the equilibrium of the reduced model (40) undergoes an instability driven by the linear effective damping, d_{eff}. For sufficiently high values of the ATP concentration parameter λ, the effective viscosity becomes

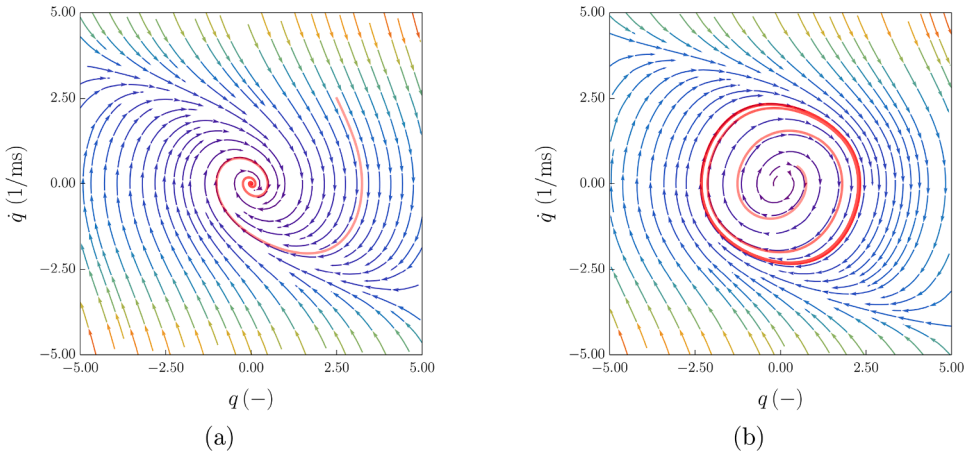

Fig. 10. Phase portraits of the 1-DOF model (40) for values of the ATP concentration parameter λ below (a) and above (b) the critical value λ_c. Background streamlines represent the vector field $(q, \dot{q})$. The red trajectory shows the dynamics of the solution associated with a perturbed initial condition. The transparency of the trajectory decreases with time. Model parameters are as in Table 2 and $S_p = 1.2$. For such values, the critical ATP concentration is $\lambda_c \approx 100$ Ns/m^2 and phase portraits are obtained for (a) $\lambda = 90$ Ns/m^2 and (b) $\lambda = 110$ Ns/m^2.

negative, i. e., energy is injected into the system and the equilibrium becomes unstable. In contrast to the LCE case, where the instability arises from an elastic-inertial feedback mediated by the jerk coefficient, the present ciliary model has no jerk, due to the absence of inertia in the passive system. In particular, a Hopf bifurcation occurs when the effective viscosity vanishes, i. e., when the ATP concentration parameter λ reaches the critical value

$$\lambda_c = \tau K + D, \tag{44}$$

which corresponds to the critical oscillation frequency

$$\omega_c = \sqrt{\frac{k_{\text{eff}}}{m_{\text{eff}}}} = \sqrt{\frac{K}{D\tau}}\,. \tag{45}$$

Due to the absence of inertia, the natural frequency ω_1 does not appear in Eq. (45), contrary to the critical frequency for the photo-deformable beam (25). The square frequency ω_c^2 at which the cilia oscillate is the characteristic chemical rate $1/\tau$ multiplied by the ratio between the effective elasticity, K, and viscosity, D, of the passive system. In this case, the chemical activity prescribes the critical oscillation frequency through the characteristic time τ, related to the binding/unbinding reaction of the motors.

Beyond the bifurcation point, the cubic dissipative term $\gamma_{\text{eff}}\dot{q}^3$ stabilizes the dynamics. The (positive) nonlinear damping counteracts the (negative) linear effective damping, yielding a supercritical Hopf bifurcation, see Appendix B. Near the bifurcation threshold λ_c, the tip angle of the cilium oscillates with amplitude

$$R(\lambda) = \varphi(L)\sqrt{\frac{4c_2}{3c_3}\frac{D\left(\lambda - \lambda_c\right)}{\mu h^2 K}}\,. \tag{46}$$

For the nonlinear dynamics, numerical simulations and phase portraits confirm the occurrence of a supercritical Hopf bifurcation at the critical values of the ATP concentration parameter λ_c predicted analytically by Eq. (44), see Fig. 10. Moreover, near the bifurcation point, the numerical results agree with the analytical predictions for both the oscillation frequency (45) and the amplitude (46), see Fig. 14.

4.2.2. *Linear stability analysis of the full linearized system*

In this section, we perform the linear stability analysis of the complete linear model (38). Analogously to the linear analysis of the photo-deformable beam of Section 3.2.2, we seek time-harmonic solutions of the form $\theta(s,t) = \tilde{\theta}(s)e^{\sigma t}$ and $f_a(s,t) = \tilde{f}_a(s)e^{\sigma t}$, for $\sigma \in \mathbb{C}$. Substituting these expressions into model (38), we find that $\tilde{f}_a = \frac{h\lambda\sigma}{\tau\sigma+1}\tilde{\theta}$ where $\tilde{\theta}(s)$ satisfies the boundary value problem

$$\begin{cases} \tilde{\theta}'''' + \chi\tilde{\theta}'' + \frac{\sigma\xi_n}{B}\tilde{\theta} = 0, \\ \tilde{\theta}(0) = 0,\ \tilde{\theta}'''(0) + \chi\tilde{\theta}'(0) = 0, \\ \tilde{\theta}'(L) = 0,\ \tilde{\theta}''(L) + \chi\tilde{\theta}(L) = 0, \end{cases} \tag{47}$$

with $\chi = \chi(\lambda,\sigma) = \frac{h^2}{B}\left(\frac{\sigma}{\tau\sigma+1}\lambda - k - \eta\sigma\right)$.

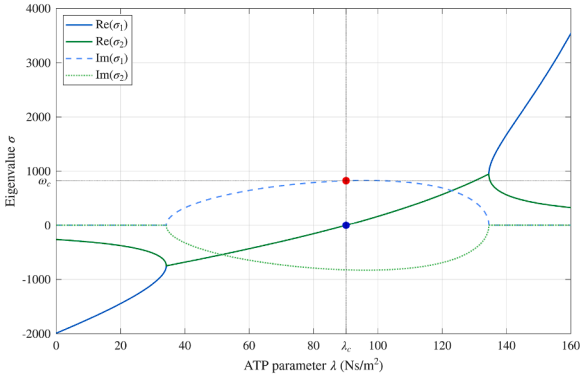

Fig. 11. Real (solid lines) and imaginary (dashed lines) parts of the eigenvalues σ_1 and σ_2, as functions of the ATP parameter λ, for a cilium with sperm number $S_p = 1.5$, and for the choice of model parameters as in Table 2. We distinguish four regions corresponding to different dynamical responses for $\theta(s,t)$: exponential decay and damped oscillations for $\lambda < \lambda_c$, and increasing oscillations and exponential growth for $\lambda > \lambda_c$.

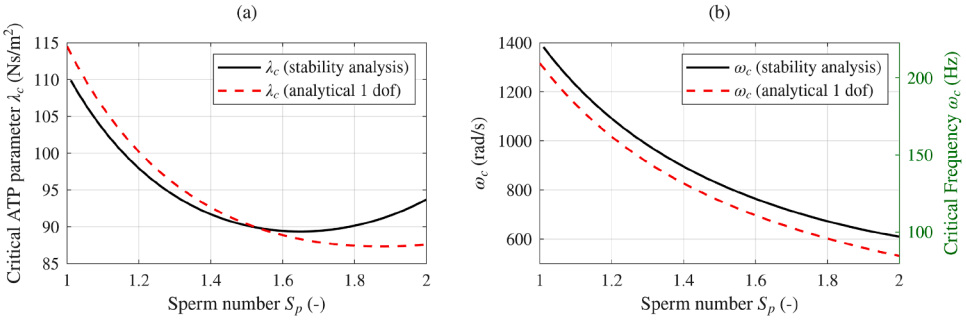

Fig. 12. Comparison of the critical ATP (a) and the critical frequency (b) for various sperm numbers using the linear stability analysis of model (36) (solid lines) and the analytical expressions (44) and (45) for the 1-DOF model (40) (dashed lines). Model parameters are as in Table 2.

We seek non-trivial solutions to (47) of the form $\bar{\theta} = \sum_{j=1}^{4} A_j e^{\beta_j s}$, where β_j are distinct roots[2] of the characteristic equation

$$\beta^4 + \chi\beta^2 + \frac{\sigma\xi_n}{B} = 0. \tag{48}$$

By imposing the boundary conditions, we get the linear system $\mathbf{MA} = \mathbf{0}$, where

$$\mathbf{M} = \begin{pmatrix} 1 & 1 & 1 & 1 \\ \beta_1 e^{\beta_1 L} & \beta_2 e^{\beta_2 L} & \beta_3 e^{\beta_3 L} & \beta_4 e^{\beta_4 L} \\ (\beta_1^2+\chi)e^{\beta_1 L} & (\beta_2^2+\chi)e^{\beta_2 L} & (\beta_3^2+\chi)e^{\beta_3 L} & (\beta_4^2+\chi)e^{\beta_4 L} \\ \beta_1(\beta_1^2+\chi) & \beta_2(\beta_2^2+\chi) & \beta_3(\beta_3^2+\chi) & \beta_4(\beta_4^2+\chi) \end{pmatrix} \tag{49}$$

As for the photo-deformable beam, the system admits nontrivial solutions if and only if $|\det \mathbf{M}(\chi(\lambda,\sigma))| = 0$, and the system dynamics about the equilibrium is determined by the real and imaginary parts of the complex zeros σ of such equation. Denoting by $\sigma_{1,2}$ the leading eigenvalues, we distinguish four regions as λ varies, see Fig. 11. For low values of λ, all eigenvalues are real and negative; as λ increases, $\sigma_{1,2}$ becomes complex and conjugate up to λ_c, when their real part changes sign, from positive to negative; finally, for higher values of λ, both eigenvalues become real and positive.

We numerically compute the zeros (λ_c, σ_c) of $\det \mathbf{M} = 0$ as functions of the sperm number S_p and show in Fig. 12 the curves of the critical ATP concentration, λ_c, and the corresponding oscillation frequency, $\omega_c = Im(\sigma_c)$. For the considered model parameters, the analytical expressions (44) and (45) for the 1-DOF model approximate the nonlinear critical values λ_c and ω_c within a relative error of 7% and 13%, respectively.

4.2.3. *Nonlinear simulations*

In this section, we explore the regime of large amplitude oscillations by solving numerically the nonlinear model (36) in COMSOL Multiphysics (see Appendix C for more details on the numerical procedure). Model parameters are reported in Table 2.

Consistent with the linear stability analysis, the computational analysis reveals the onset of a limit cycle as the ATP parameter exceeds the critical value λ_c, thus confirming a Hopf-like supercritical bifurcation.

[2] There is also the possibility of two repeated roots, each with multiplicity two. In that case, the solution reduces to $\tilde{\theta} = 0$.

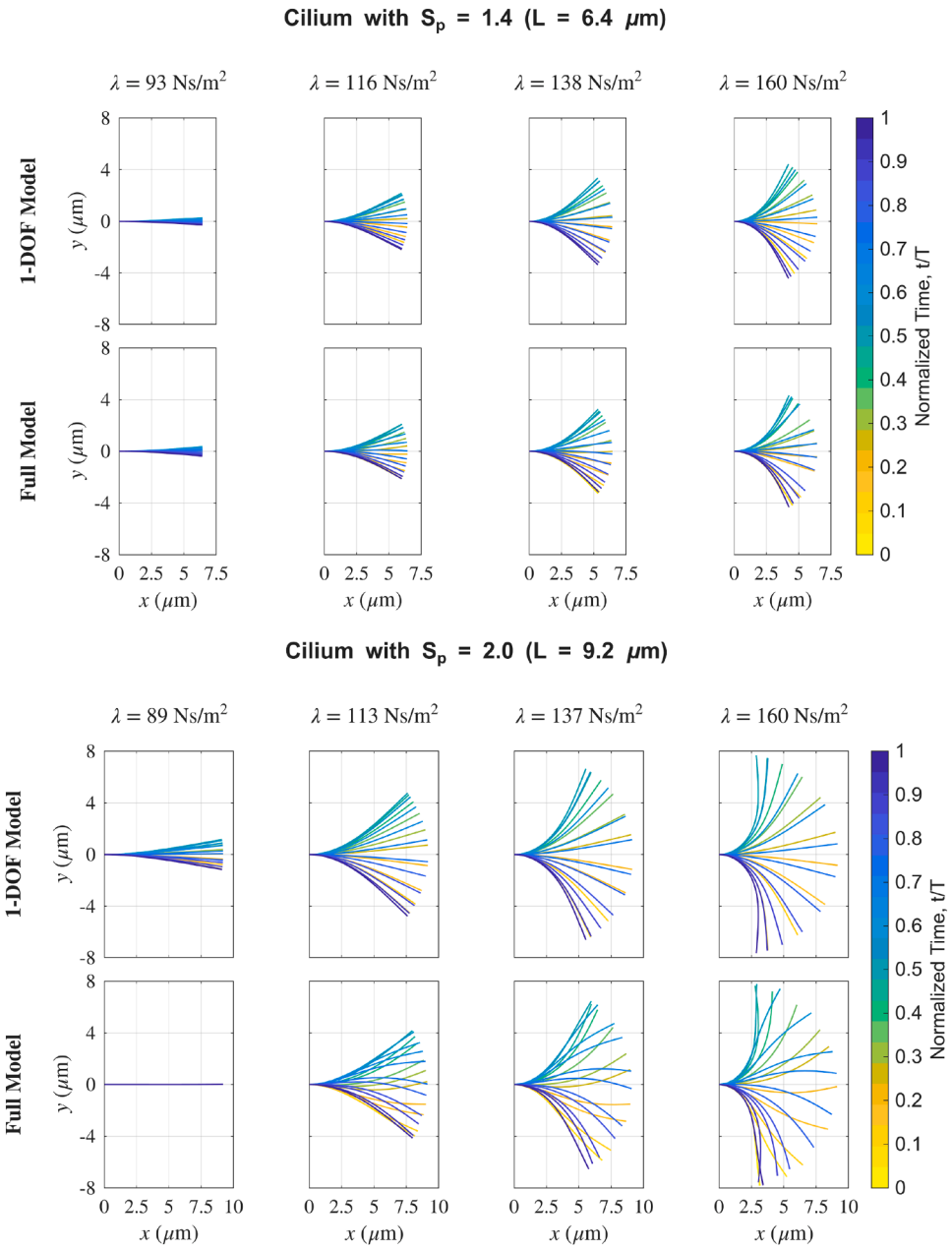

Fig. 13. Comparison of cilium shapes between 1-DOF model (40) and full model (36) for different values of the ATP parameters λ, increasing from left to right. The sperm number is $S_p = 1.4$ (top) and $S_p = 2$ (bottom), while other model parameters are as in Table 2. Colors denote the normalized time t/T where T is the oscillation period.

Finally, we analyze the features of the periodic solutions obtained by the 1-DOF model (40) compared to the full model (36). In particular, we focus on three aspects: the beating frequency ω, the maximum tip angle $\theta(L)$, and the time evolution of the cilium configurations. In Figs. 14 and 13, we show the results for selected values of the sperm number. We conclude that the 1-DOF model correctly retains all essential features of the full model.

5. Discussion

We have formulated and analyzed reduced-order models for two classes of chemomechanically coupled, active elastic filamentous structures: photochemically deformable LCE rods driven by external illumination, and eukaryotic cilia with ATP-powered internal

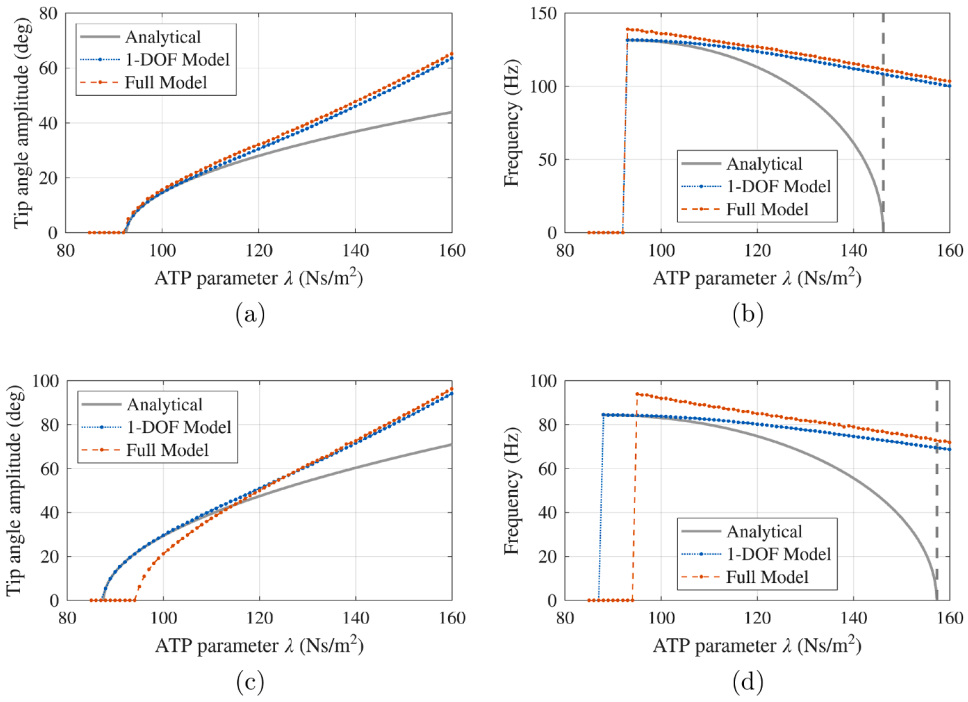

Fig. 14. Comparison between 1-DOF model (40) in blue and full model (36) in orange for (a,c) the amplitude of the tip angle $\theta(L)$ and (b,d) the oscillation frequency ω, by increasing the ATP parameter λ. Numerical simulations are compared to analytical results in gray: (a,c) tip angle amplitude given by Eq. (46) and (b,d) imaginary part of leading eigenvalues $\omega(\lambda) = \omega_c\sqrt{1-(\lambda-\lambda_c)^2/(4\tau DK)}$ for $\lambda \geq \lambda_c$. The sperm number is $S_p = 1.4$ (a,b) and $S_p = 2$ (c,d), while other model parameters are as in Table 2. Maximum tip angles and oscillation frequencies are extracted from periodic oscillations after the initial transient regime.

molecular motors. Using the unified mechanical framework of active planar rods, we highlight commonalities and differences between the two systems.

For both systems, we extract the essential physical mechanisms that trigger their oscillatory instabilities by proposing simplifications of the state-of-the-art models. For the LCE system, we assume a low concentration of cis-isomers and neglect self-shadowing effects, which allows us to treat the light stimulus as a local boundary condition without solving the geometric optics equations in a deforming, a-priori unknown domain. In particular, we simplified the description of light attenuation and propagation by neglecting light refraction, which could be modelled more accurately as in Goriely et al. (2023). For the ATP-powered cilia, we employ an explicit local feedback law between active forces and sliding to replace the PDEs that govern the mechanochemistry of molecular motors and their binding/unbinding kinetics. Such simplifications also define the limitations of our reduced models, which are valid in specific regimes. For photo-responsive LCEs, we neglect self-shadowing effects, restricting validity to short beams (Appendix A.3.1), and we assume small light penetration depth and fast cis-to-trans relaxation times. For cilia, we adopt the Resistive Force Theory assuming that viscous forces are purely local, thus omitting long-range hydrodynamic coupling. Moreover, both models are constrained to planar kinematics, precluding potential three-dimensional waveforms and effects. Finally, the derivation of 1-DOF models via single-mode truncation provides asymptotic approximation near the bifurcation, without explicitly quantifying the errors arising from neglected higher-order modes.

Our analysis culminates in the derivation of one-degree-of-freedom models. While the reduction to 1-DOF oscillators is the expected result for a system undergoing a Hopf bifurcation where a single mode becomes unstable (as described by the center-manifold theory), the physical significance of our reduced models lies in their ability to capture the system-specific mechanochemical couplings. From the 1-DOF models, we obtain explicit formulas for key quantities such as critical activation thresholds, critical beating frequencies ω_c, and oscillation amplitudes near the onset of the Hopf instability. These formulas provide a direct, quantitative description of the effect of the control parameters (light intensity or ATP concentration) on observable features of the oscillations. The accuracy of the 1-DOF models in predicting such features, when compared to the complete nonlinear models (see Sections 3.2.3 and 4.2.3), confirms that they preserve the relevant mechanochemical physics in the asymptotic regime near the bifurcation. Both 1-DOF models yield an effective oscillator for which the critical frequency is the resonance frequency

$$\omega_c^2 = k_{\text{eff}}/m_{\text{eff}},$$

where m_{eff} and k_{eff} are, respectively, the effective inertia and elasticity, which include contributions from the active components of the system. In particular, for the light-powered oscillations of the LCE filaments,

$$\omega_c^2 = \frac{K + D/\tau}{M} \approx \omega_1^2 + \frac{1}{\tau^2}\frac{\tau D}{M},$$

where τ is the characteristic relaxation time for the cis-to-trans chemical reaction, and M, K, and D are respectively the effective inertia, elasticity, and viscosity of the passive system. This critical beating frequency is set by the balance between inertia and elasticity, where the effective elastic modulus arises from bending stiffness corrected by a term D/τ due to the evolution of spontaneous curvature, modulated by the characteristic chemical cis lifetime τ. In interpreting self-oscillating LCE cantilevers, the observed frequencies have often been compared to the first fundamental frequency, ω_1, on an empirical basis, showing discrepancies. The formula above provides a rationale for the difference between the critical frequency, ω_c, and the first fundamental frequency, ω_1, in the case of photochemical actuation. A caveat is that the formula above applies only at the onset of the bifurcation (not for the limit cycle when the activation parameter is far from threshold) and for short enough rods, so that self-shadowing can be neglected.

For the ATP-fueled eukaryotic cilia,

$$\omega_c^2 = \frac{K}{D\tau} = \frac{1}{\tau^2}\frac{\tau K}{D},$$

where K and D are respectively the effective elasticity and damping of the passive system, and τ is the characteristic time for the chemical reaction that governs the binding/unbinding of the molecular motors. This critical beating frequency is set by the balance between elasticity and dissipation, where the effective viscous parameter D is modulated by the characteristic chemical switching time τ.

In both systems, the analytical formulas for the amplitude show that limit cycles grow proportionally to the square root of the distance between the bifurcation parameter and its critical value, consistent with the general structure of Hopf bifurcations.

The one-degree-of-freedom models provide a unifying mechanochemical perspective through which the two models can be compared to highlight differences and similarities of the underlying activation mechanisms. Despite the common mathematical structure, i. e., nonlinear oscillators undergoing a Hopf bifurcation, the physical origins of oscillations are fundamentally different, as summarized in Table 3. Indeed, both systems are described by the rod theory but the feedback mechanisms are not interchangeable: in LCEs, the spontaneous curvature evolves with the tangent angle, providing a position-dependent feedback, while for cilia, the active motor force evolves with the rate of the tangent angle, providing a velocity-dependent feedback. Therefore, for LCEs, self-sustained oscillations emerge as a fundamentally inertial phenomenon. Through the light-powered activity, the presence of inertia in the passive system gives rise to an effective jerk, by which the inertia is coupled to the effective elasticity over the timescale of the cis-to-trans chemical reaction. The instability is driven by such a coupling, and the oscillation frequency results from an elasticity-inertia balance. In contrast, for cilia, the effective jerk term is absent, and the instability cannot be driven by elasticity. Instead, chemical activity modulates the effective damping, which becomes negative at high ATP concentration, hence providing a motive force. Here, oscillations are the result of an elasticity-damping balance. In both cases, nonlinear terms have stabilizing effects: for LCEs, a cubic stiffness counteracts the linear one; for cilia, a cubic (positive) damping opposes the negative damping driven by ATP. Hence, both instabilities arise due to a linear coefficient that is destabilizing (stiffness or damping), and limit cycles emerge as a consequence of a corresponding nonlinear term of opposite sign. Moreover, in both systems, activity affects the oscillatory dynamics through the characteristic time of the chemical reactions controlling the chemo-mechanical feedback. This shows that the oscillations in these Hopf-type instabilities represent a mechanochemical phenomenon different from purely mechanical resonance, where the frequency would be dictated solely by the passive structural properties.

We believe that the delay-driven instabilities explored in this study could provide valuable insight into general principles for designing and understanding self-oscillating systems in active matter. A promising avenue for future research is to compare these findings with analogous phenomena observed in distinct active systems, such as plants (Agostinelli et al., 2020, 2021a,b). Moreover, future work is needed to elucidate the mechanisms for wavelength selection in both ATP-driven cilia and photo-deformable LCE systems, which remain poorly understood at present (Lee et al., 2025).

CRediT authorship contribution statement

Daniele Agostinelli: Writing – review & editing, Writing – original draft, Methodology, Investigation, Formal analysis, Data curation, Conceptualization; **Irene Anello:** Writing – review & editing, Writing – original draft, Methodology, Investigation, Formal analysis, Data curation, Conceptualization; **Reza Norouzikudiani:** Writing – review & editing, Writing – original draft, Methodology, Investigation, Formal analysis, Data curation, Conceptualization; **Antonio DeSimone:** Writing – review & editing, Writing – original draft, Supervision, Methodology, Investigation, Funding acquisition, Formal analysis, Data curation, Conceptualization.

Data availability

Data will be made available on request.

Declaration of competing interest

The authors declare that they have no known competing financial interests or personal relationships that could have appeared to influence the work reported in this paper.

Acknowledgments

Support for this research was provided by the European Union's Horizon Europe research and innovation programme under grant agreement N° 101,046,846 (Mapworms) and by the Italian Ministry of Research through the projects Response (PRIN 2020) and Abyss (PRIN 2022).

Appendix A. Models for LCE photo-deformable beams

In Appendix A.1, we introduce a general model for LCE beams, which accounts for both the cis-fraction dynamics and the light illumination, including self-shadowing effects. In Appendix A.2, in the limit of small cis-fraction, we show how to derive the simplified model (10) presented in the main text. Finally, in Appendix A.3, we use numerical simulations to investigate the applicability of neglecting self-shadowing effects and assuming small cis-fractions.

A.1. The general model

Similarly to the main text, we model the LCE beam as a planar rod. Here, however, we consider the rod extensible. We denote by $s \in [0, L]$ the arc-length coordinate in the undeformed reference configuration, and by $S \in [0, \ell(t)]$ the arc-length coordinate in the deformed configuration at time t, where $\ell(t)$ is the total length. The axial stretch of the midline is $\lambda_s(s,t) = S'(s,t)$, and the kinematics relation (2) is generalized to $\mathbf{r}'(s,t) = \lambda_s(s,t)\mathbf{t}(s,t)$ so that Eq. (3) becomes

$$\begin{cases} M'(s,t) + \lambda_s(s,t)(\mathbf{t}(s,t) \times \mathbf{R}(s,t)) \cdot \mathbf{e}_3 + m(s,t) = 0, \\ \mathbf{R}'(s,t) + \mathbf{g}(s,t) = 0. \end{cases} \tag{A.1}$$

The inextensible case is recovered by imposing $s = S$, i. e., $\lambda_s = 1$.

Moreover, instead of prescribing an evolution law for the spontaneous curvature κ_0, we explicitly define its relationship with the fraction of cis molecules n_c as

$$\kappa_0(s,t) = -\frac{12}{h^3} \int_{-h/2}^{h/2} \epsilon_p(s,t,z) z \, dz, \tag{A.2}$$

where $\epsilon_p(s,t,z) = -c n_c(s,t,z)$ is the spontaneous strain, which is linearly proportional, through the constant c, to the fraction of cis molecules $n_c(s,t,z)$ and only accounts for photochemical effects. z denotes the coordinate across the thickness of the beam (in the normal direction $\mathbf{n}$), with $z \in [-h/2, h/2]$. In turn, the cis-fraction $n_c(s,t,z)$ depends on the light intensity that reaches each point z along the thickness at time t, $J(\theta(s,t), z)$, through the evolution equation

$$\dot{n}_c(s,t,z) = \Gamma J(\theta(s,t), z)\big(1 - n_c(s,t,z)\big) - \frac{1}{\tau} n_c(s,t,z), \tag{A.3}$$

where τ is the cis-lifetime (the characteristic relaxation time back to the steady trans state), and Γ is the material absorption constant such that $\Gamma J(\theta(s,t), z)$ represents the rate of formation of cis-molecules.

To close the system, we model $J(\theta, z)$ through the generalized Beer-Lambert law, which describes light attenuation in z due to photon absorption, i. e.,

$$\begin{cases} \frac{\partial J}{\partial z}(\theta, z) = -\mathrm{sgn}(\theta) \frac{1 - n_c}{d} J(\theta, z), & z \in \left[-\frac{h}{2}, \frac{h}{2}\right], \\ J(\theta, z) = \mathrm{sgn}(\theta) \bar{J} \sin(\theta), & z = -\mathrm{sgn}(\theta)\frac{h}{2}, \end{cases} \tag{A.4}$$

where d is the penetration depth, and the sign function (sgn) determines the direction of light propagation along z with the proper boundary condition. Since our goal is to capture the essential qualitative mechanism driving the deformation, we assumed an exponential decay of the light intensity along the normal direction to the surface, even though the actual light propagation inside the material is more complex. A more accurate treatment of the illumination, especially when the incident light is not aligned with the surface normal, would require explicitly accounting for refraction inside the material. To consider this effect, one would follow the procedure proposed by Goriely et al. (2023), in which the refraction of light rays inside the material is explicitly included.

In summary, the most general model consists of Eqs. (A.1), (5), (7), (8), (A.2), (A.3), (A.4), and boundary conditions (4), namely,

$$\begin{cases} B\big(\theta''(s,t) - \kappa_0'(s,t)\big) + \lambda_s(s,t)(\mathbf{t}(s,t) \times \mathbf{R}(s,t)) \cdot \mathbf{e}_3 - \rho I \ddot{\theta}(s,t) = 0, \\ \mathbf{R}'(s,t) = D\dot{\mathbf{r}}(s,t) + \rho A \ddot{\mathbf{r}}(s,t), \\ \kappa_0(s,t) = \frac{12c}{h^3} \int_{-h/2}^{h/2} n_c(s,t,z) z \, dz, \\ \dot{n}_c(s,t,z) = \Gamma J(\theta(s,t), z)\big(1 - n_c(s,t,z)\big) - \frac{1}{\tau} n_c(s,t,z), \\ \frac{\partial J}{\partial z}(\theta, z) = -\mathrm{sgn}(\theta) \frac{1 - n_c}{d} J(\theta, z), \\ J\left(\theta, -\mathrm{sgn}(\theta)\frac{h}{2}\right) = \mathrm{sgn}(\theta) \bar{J} \sin(\theta), \\ \theta(0,t) = 0, \quad \dot{\mathbf{r}}(0,t) = \mathbf{0}, \\ \mathbf{R}(L,t) = \mathbf{0}, \quad M(L,t) = 0. \end{cases} \tag{A.5}$$

A.2. The simplified model for $n_c \ll 1$

Let us now consider the low n_c regime ($n_c \ll 1$). In this limit, the spontaneous strain $\epsilon_p(z) = -cn_c(z)$ is small in magnitude and its average produces negligible axial strain. However, spatial variations of $\epsilon_p(z)$ across the thickness can produce appreciable curvatures. Hence, it is consistent to treat the beam as inextensible ($\lambda_s = 1$) while modeling the curvature induced by the cis-fraction n_c, whose evolution Eq. (A.3) can be simplified to

$$\dot{n}_c(s,t,z) = \Gamma J(\theta(s,t),z) - \frac{1}{\tau} n_c(s,t,z). \tag{A.6}$$

In particular, for $n_c \ll 1$, Eq. (A.4) can be approximated by

$$\begin{cases} \frac{\partial J}{\partial z}(\theta,z) = -\frac{\mathrm{sgn}(\theta)}{d} J(\theta,z), & z \in \left[-\frac{h}{2}, \frac{h}{2}\right], \\ J(\theta,z) = \mathrm{sgn}(\theta)\bar{J}\sin(\theta), & z = -\mathrm{sgn}(\theta)\frac{h}{2}, \end{cases} \tag{A.7}$$

which has the analytical solution

$$J(\theta,z) = \mathrm{sgn}(\theta)\bar{J}\sin\theta \exp\left(-\frac{\mathrm{sgn}(\theta)z + h/2}{d}\right). \tag{A.8}$$

In summary, the model for $n_c \ll 1$ consists of Eqs. (3), (5), (7), (8), (A.2), (A.6), (A.8), and boundary conditions (4), that is,

$$\begin{cases} B\left(\theta''(s,t) - \kappa_0'(s,t)\right) + \lambda_s(s,t)(\mathbf{t}(s,t)\times\mathbf{R}(s,t))\cdot\mathbf{e}_3 - \rho I\ddot{\theta}(s,t) = 0, \\ \mathbf{R}'(s,t) = D\dot{\mathbf{r}}(s,t) + \rho A\ddot{\mathbf{r}}(s,t), \\ \kappa_0(s,t) = \frac{12c}{h^3}\int_{-h/2}^{h/2} n_c(s,t,z)z\,dz, \\ \dot{n}_c(s,t,z) = \Gamma J(\theta(s,t),z) - \frac{1}{\tau}n_c(s,t,z), \\ J(\theta,z) = \mathrm{sgn}(\theta)\bar{J}\sin\theta\exp\left(-\frac{\mathrm{sgn}(\theta)z+h/2}{d}\right), \\ \theta(0,t) = 0, \quad \dot{\mathbf{r}}(0,t) = \mathbf{0}, \\ \mathbf{R}(L,t) = \mathbf{0}, \quad M(L,t) = 0. \end{cases} \tag{A.9}$$

In conclusion, we note that system (A.9) can be written as (10) in the main text. Indeed, by combining the time derivative of Eq. (A.2) with Eq. (A.6), we obtain the evolution law for κ_0

$$\dot{\kappa_0}(s,t) = -\frac{1}{\tau}\kappa_0(s,t) + \frac{12c\Gamma}{h^3}\int_{-h/2}^{h/2} J(\theta(s,t),z)z\,dz. \tag{A.10}$$

Hence, substituting the analytical solution (A.8) for $J(\theta,z)$, we obtain the simplified evolution law (9) in the main text, i. e.,

$$\dot{\kappa_0} = -\frac{1}{\tau}\kappa_0 - \frac{12c\Gamma\beta}{h^3}\bar{J}\sin\theta, \tag{A.11}$$

with $\beta = -d(d - h/2 - \exp(-h/d)(d + h/2)) > 0$.

A.3. Numerical simulations

In this section, we assess the accuracy and range of applicability of the approximations made to derive the models (A.5) and (A.9): neglecting self-shadowing effects (Appendix A.3.1) and assuming $n_c \ll 1$ (Appendix A.3.2).

We solve numerically systems (A.5) and (A.9) for the unknown variables (n_c, J, $\mathbf{r}$, θ, $\mathbf{R}$, M, λ_s, κ_0), as detailed in Appendix C. Material and geometric parameters are reported in Table 1 in the main text.

A.3.1. The effect of self-shadowing

The region unexposed to light due to self-shadowing is determined using geometric optics equations, solved through the `heat radiation` module of COMSOL Multiphysics (Norouzikudiani et al., 2024). In this framework, the beam model is coupled with a 2D simulation that tracks the mid-axis positions and tangent angles. The light propagation is then solved within the 2D domain to evaluate the intensity distribution along the beam boundary, which is continuously updated based on the beam dynamics. At points obscured by self-shadowing, the incident light intensity vanishes instead of being enforced by the boundary conditions in (A.4). This updated boundary condition is fed back into the beam model to solve the deformation and self-oscillation dynamics.

As shown in Fig. A.1, the critical intensity predicted by the model without self-shadowing is in agreement with that of the model including self-shadowing for beam lengths up to 20 mm. However, for longer beams, predictions diverge, and the model without self-shadowing underestimates the critical intensity.

To clarify the cause of this discrepancy, we examine snapshots of the beam profile at different phases of an oscillation cycle for varying beam lengths, shown in Fig. A.2. For beam lengths up to 20 mm, oscillations occur primarily in the first mode, making the self-shadowing effect negligible. However, as the beam length increases beyond 20 mm, higher oscillation modes become more prominent, and the impact of self-shadowing becomes more significant.

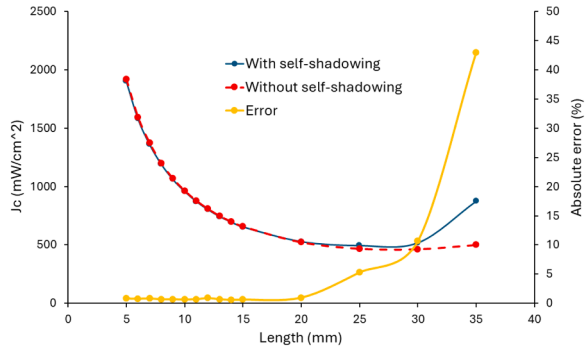

Fig. A.1. Comparison of critical intensities using the nonlinear model (A.5) with and without self-shadowing for various beam lengths.

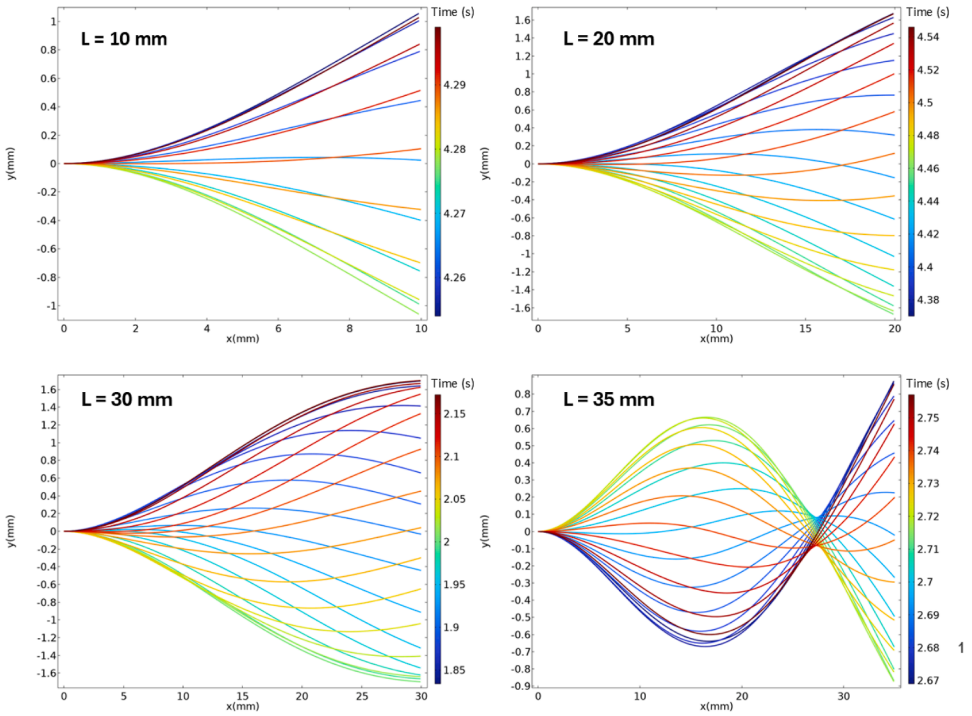

Fig. A.2. Snapshots of the beam profile at different times for various lengths using the nonlinear model (A.5) with self-shadowing.

We further conduct parametric studies for different light intensities at a beam length of 20 mm, near the maximum length for which the absolute error between the predicted critical intensities is less than 1.5%. This analysis assesses the capability of the non-shadowing model to accurately reproduce oscillation amplitude and frequency. Indeed, the results in Fig. A.3 show good agreement between the two models, even at high light intensities.

In conclusion, these results motivate and justify the use of models without self-shadowing for beams of length $L \leq 20$ mm.

A.3.2. Small n_c approximation

In this section, we focus on the effect of the small n_c assumption on the light-powered oscillations, restricting ourselves to the non-shadowing regime discussed in Appendix A.3.1, i. e., $L \leq 20$ mm. We analyze the critical light intensity and oscillation frequency by comparing the full model (A.5) with the reduced model for small n_c (A.9), and its linearization (14). As shown in Fig. A.4, the linearized model (14) predicts decreasing critical intensity and oscillation frequency with increasing length, in good agreement with both nonlinear formulations (A.5) and (A.9).

For a beam of length $L = 10$ mm, we investigate self-sustained oscillations under varying light intensities using the nonlinear models (A.5) and (A.9). In both cases, the oscillation amplitude increases with light intensity (Fig. A.5a). However, the small n_c model becomes less accurate at high light intensities. This discrepancy arises because, near the critical intensity, the fraction of cis molecules remains small, aligning with our assumptions, but at higher intensities, the simplified model overestimates the cis fraction,

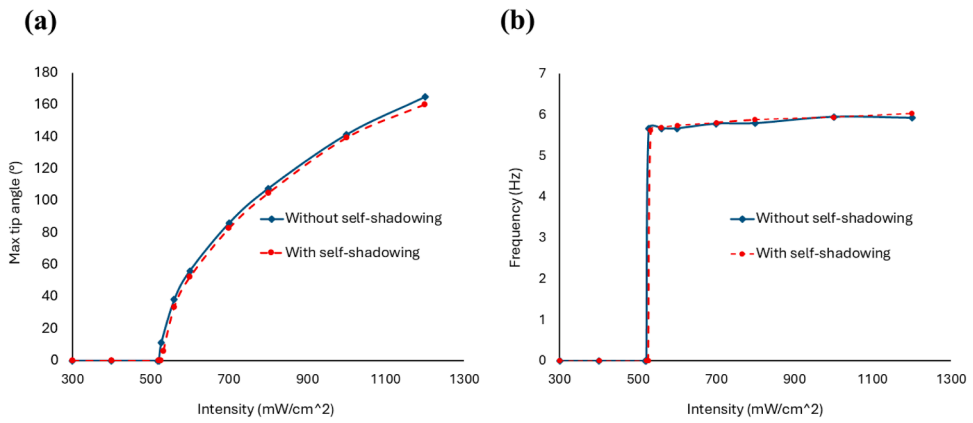

Fig. A.3. Maximum tip angle (a) and oscillation frequency (b) for different light intensities applied to a beam of length $L = 20$ mm, using the nonlinear model (A.5) with and without self-shadowing.

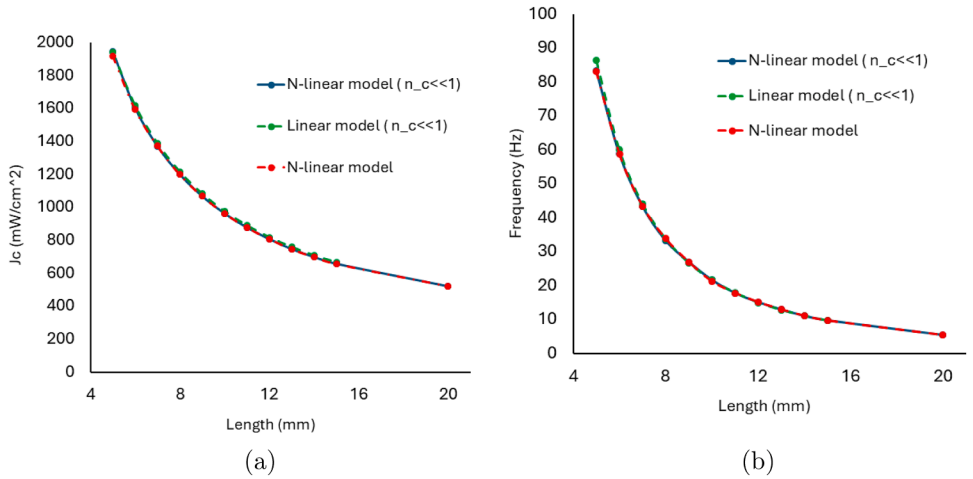

Fig. A.4. Comparison of the critical intensity (a) and the critical frequency (b) for various beam lengths using the full model (A.5), the reduced model for low n_c (A.9), and its linearization (14).

sometimes exceeding its physical upper limit of 1 (Fig. A.5c). In contrast, the oscillation frequency is nearly identical in both models and remains almost constant throughout the tested interval (Fig. A.5b).

In conclusion, for $L \leq 20$ mm and in the vicinity of the critical light intensity $\bar{J}_c$, the small-n_c assumption provides an accurate description of the photo-deformable LCE beam. Moreover, as illustrated in Fig. A.2, approximating the solution θ of Eq. (13) by the first-mode truncation $\theta(s,t) = \varphi(s)q(t)$, where $\varphi(s)$ is given by Eq. (17), is well supported by the graphical evidence. These results provide the insight to derive the 1-DOF model (20) in the main text.

Appendix B. Stability analysis of 1-DOF models

In this section, we study the one-degree-of-freedom (1-DOF) models for photo-deformable beams (Section 3.1.2) and ATP-driven cilia (Section 4.1.2), both of which have the form of a nonlinear oscillator

$$a\dddot{x} + m\ddot{x} + d\dot{x} + kx + H(x,\dot{x}) = 0, \qquad a, d \geq 0,\ m, k > 0 \tag{B.1}$$

with equilibrium at $x(t) \equiv 0$. The nonlinear term $H(x,\dot{x})$ depends on the specific model, while the linear terms are

- kx, a spring-like restoring force (elasticity),
- $d\dot{x}$, a dashpot-like term representing viscous dissipation (damping),
- $m\ddot{x}$, the resistance to acceleration (inertia),
- $a\dddot{x}$, a jerk-proportional term that introduces a frequency-dependent negative damping.

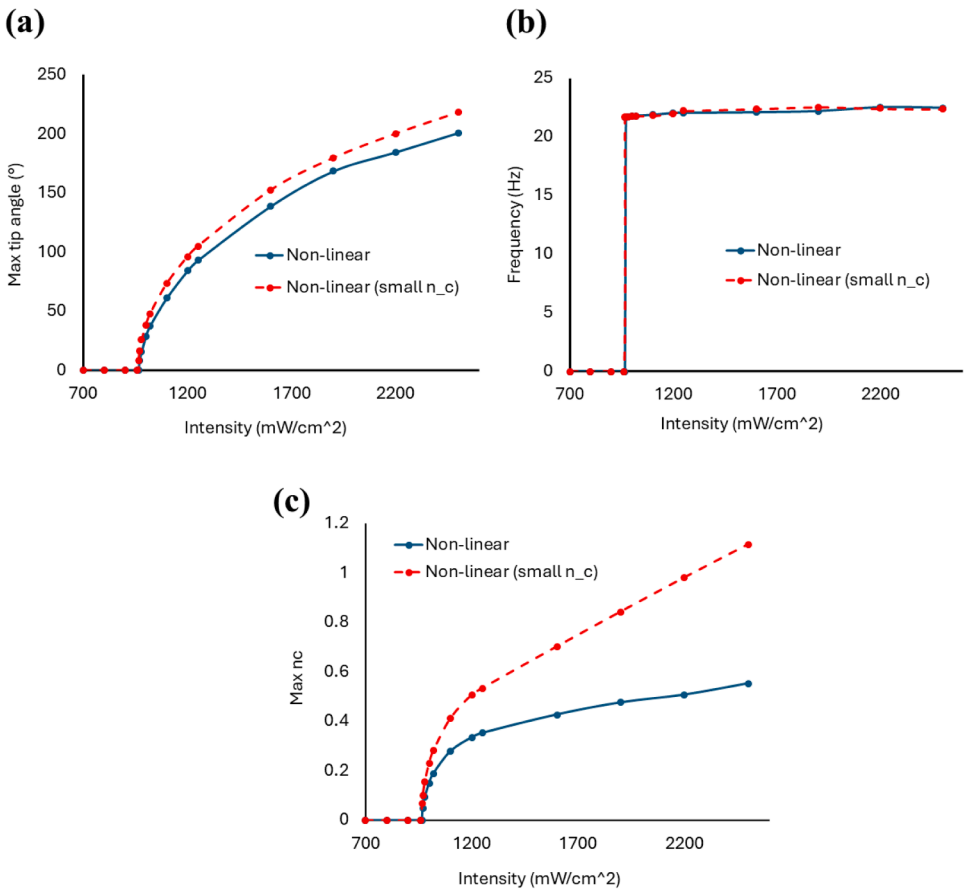

Fig. A.5. Maximum tip angle (a), oscillation frequency (b), and maximum fraction of cis molecules (c) for different light intensities applied to a beam of length $L = 10$ mm, using nonlinear models (A.5) and (A.9) (without self-shadowing effect).

B.1. Linear Stability and Hopf Bifurcation

The stability of the trivial equilibrium is determined by the eigenvalues of the linearized system, i. e., by the roots of the characteristic equation:

$$a\lambda^3 + m\lambda^2 + d\lambda + k = 0. \tag{B.2}$$

By the Routh-Hurwitz criterion, all eigenvalues have negative real part if and only if

$$\alpha := ak - dm < 0. \tag{B.3}$$

At $\alpha = 0$, a pair of complex conjugate eigenvalues crosses the imaginary axis with nonzero velocity, $\lambda_{1,2} = \pm i\omega_c$ where $\omega_c = \sqrt{k/m}$ is the critical frequency. Moreover, if $a \neq 0$, the remaining eigenvalue is real and strictly negative, $\lambda_3 = -m/a < 0$. Thus, a Hopf bifurcation occurs when $\alpha = 0$ and the equilibrium is stable for $\alpha < 0$ and unstable for $\alpha > 0$.

B.2. Normal form reduction and bifurcation analysis

To determine the bifurcation type (supercritical, subcritical, or degenerate), we compute the first Lyapunov coefficient following Kuznetsov (2023). Near the bifurcation point $\alpha = 0$, the dynamics is confined to a 2D center manifold and can be described by a single complex variable, $z(t) \in \mathbb{C}$. The normal form of the Hopf bifurcation is

$$\dot{z} = (\sigma(\alpha) + i\omega(\alpha))z + C_1(\alpha)z|z|^2 + O(|z|^4) \tag{B.4}$$

where $\sigma(0) = 0$, $\omega(0) = \omega_c$, and C_1 is a complex coefficient determined by the nonlinearities of the system. Since z is a coordinate in the center manifold with an amplitude that is half of the physical variable x, we can rewrite the canonical equation by introducing polar coordinates $z = (r/2)e^{i\phi}$, i. e.,

$$\begin{cases} \dot{r} &= \sigma(\alpha)r + \mathrm{Re}(C_1(\alpha))r^3/4, \\ \dot{\phi} &= \omega(\alpha) + \mathrm{Im}(C_1(\alpha))r^2/4, \end{cases} \tag{B.5}$$

and the first Lyapunov coefficient is defined as $\ell_1 := \mathrm{Re}(C_1(0))/\omega(0)$. If $\ell_1 < 0$, the Hopf bifurcation is supercritical and a unique stable limit cycle emerges with steady-state amplitude

$$r_0^2(\alpha) = \frac{-4\sigma(\alpha)}{\mathrm{Re}(C_1(\alpha))} \approx \frac{-4\sigma(\alpha)}{\omega_c \ell_1} \tag{B.6}$$

for small $\alpha > 0$. If $\ell_1 > 0$, the Hopf bifurcation is subcritical. In the following, we show the analysis for the two particular cases of interest.

1. **Photo-responsive LCE beams.** The 1-DOF model is the third-order system ($a \neq 0$) with $H(x, \dot{x}) = -\gamma x^3$ for $\gamma > 0$, i. e., the cubic stiffness acts as a softening nonlinearity. As described in Section 3.1.2, both the effective elasticity, k, and the nonlinear coefficient, γ, depend on the light intensity and represent the active component of the system. Expressing k in terms of α, perturbation analysis yields a pair of conjugate eigenvalues $\lambda_{1,2} = \pm i\omega(\alpha)$, where

$$\sigma(\alpha) = \frac{\alpha}{2\left(ad + m^2\right)} + o(\alpha), \qquad \omega(\alpha) = \sqrt{\frac{d}{a}}\left(1 + \frac{\alpha m}{2d\left(ad + m^2\right)}\right) + o(\alpha), \tag{B.7}$$

and the third eigenvalue

$$\lambda_3 = -\frac{m}{a} - \frac{\alpha}{ad + m^2} + o(\alpha). \tag{B.8}$$

We use the combined reduction/normalization technique (Section 5.4 in Kuznetsov, 2023) to compute the first Lyapunov coefficient as

$$\ell_1 = -\frac{3\gamma}{2a\omega_c\left(\omega_c^2 + m^2/a^2\right)}, \tag{B.9}$$

where $\omega_c = \omega(0) = \sqrt{d/a}$. Since $\ell_1 < 0$ for $\gamma > 0$, the Hopf bifurcation is supercritical and, by Eq. (B.6), the resulting limit cycle has amplitude

$$r_0^2(\alpha) \approx \frac{4\alpha}{3a\gamma} \tag{B.10}$$

for small $\alpha > 0$.

2. **ATP-driven cilia.** The 1-DOF model is the second-order system ($a = 0$) with $H(x, \dot{x}) = \gamma \dot{x}^3$, for $\gamma > 0$, i. e., a positive cubic damping. As described in Section 4.1.2, the effective damping, d, embeds the chemical activity. In this case $\alpha = -dm$, and the eigenvalues are $\lambda_{1,2} = \sigma(\alpha) \pm i\omega(\alpha)$, where

$$\sigma(\alpha) = \frac{\alpha}{2m^2} \quad \text{and} \quad \omega(\alpha) = \sqrt{\frac{k}{m} - \sigma(\alpha)^2}. \tag{B.11}$$

Using the normal form method (Section 3.5 in Kuznetsov, 2023), we find that the first Lyapunov coefficient is

$$\ell_1 = -\frac{3c\omega_c}{2m}, \tag{B.12}$$

where $\omega_c = \omega(0) = \sqrt{k/m}$. Since $\ell_1 < 0$ for $\gamma > 0$, the Hopf bifurcation is supercritical and, by Eq. (B.6), the amplitude of the limit cycle is

$$r_0^2(\alpha) \approx \frac{4\alpha}{3\gamma k} \tag{B.13}$$

for small $\alpha > 0$.

Appendix C. Numerical implementation and weak forms

In this appendix, we detail the numerical procedures to solve the simplified models (10) for LCE rods and (36) for ATP-driven cilia (Appendix C.1), and the general model (A.5) for LCE rods (Appendix C.2). For all models, we employ the finite element method, implemented via the `Weak Form PDE` and `Domain ODEs and DAEs` interfaces in COMSOL Multiphysics.

C.1. Implementation of the simplified nonlinear models

For the kinematics relations and mechanical balance, we introduce the test fields $\tilde{\theta}$, $\tilde{\mathbf{r}}$, $\tilde{\mathbf{R}}$ associated with the tangent angle $\theta(s,t)$, position $\mathbf{r}(s,t)$, and internal force $\mathbf{R}(s,t)$, respectively. Accounting for the natural condition $\theta'(L,t) = \kappa_0(L,t)$, and the essential conditions $\tilde{\theta}(0,t) = 0$, $\tilde{\mathbf{r}}(0,t) = \mathbf{0}$ and $\tilde{\mathbf{R}}(L,t) = \mathbf{0}$, we derive the weak forms of Eqs. (2)–(3) as

$$\begin{aligned}
&\int_0^L (\mathbf{r}' - \mathbf{t}) \cdot \tilde{\mathbf{r}}\, ds = 0,\\
&\int_0^L \left[-B(\theta' - \kappa_0)\tilde{\theta}' + \left((\mathbf{t} \times \mathbf{R}) \cdot \mathbf{e}_3\right)\tilde{\theta} + m\tilde{\theta}\right] ds = 0,\\
&\int_0^L (\mathbf{R}' + \mathbf{g}) \cdot \tilde{\mathbf{R}}\, ds = 0.
\end{aligned} \tag{C.1}$$

where, for LCE rods, $m = -\rho I \ddot{\theta}$ and $\mathbf{g} = -D\dot{\mathbf{r}} - \rho A \ddot{\mathbf{r}}$, while for cilia, $\kappa_0 = 0$, $m = -h\big(kh\theta + \eta h\dot{\theta} - f_a\big)$, and $\mathbf{g} = -\xi_n(\mathbf{n}\cdot\dot{\mathbf{r}})\mathbf{n} - \xi_t(\mathbf{t}\cdot\dot{\mathbf{r}})\mathbf{t}$. For the space discretization, we use linear or quadratic Lagrange shape functions. We implement these weak form equations in COMSOL through the `Weak Form PDE` interface.

For the active variables - spontaneous curvature $\kappa_0(s,t)$ for LCEs and active motor force $f_a(s,t)$ for cilia - we use the `Domain ODEs and DAEs` interface to discretize them in space by quadratic discontinuous Lagrange shape functions. We couple monolithically the weak forms (C.1) to the evolution laws

$$\text{LCE:}\quad \dot{\kappa}_0 = -\frac{\kappa_0}{\tau} - \lambda\overline{J}\sin\theta, \tag{C.2}$$

$$\text{Cilia:}\quad \dot{f}_a = -\frac{1}{\tau}\big(f_a - \lambda h\dot{\theta} + \mu\tau(h\dot{\theta})^3\big). \tag{C.3}$$

Finally, we integrate in time using the Generalized-α method for the case of LCE rods, and the BDF method for the case of cilia.

C.2. Implementation of the general model for LCE rods

As discussed in Appendix A, the general model (A.5) for LCE rods accounts for axial extensibility and depth-dependent photochemistry. Therefore, we modify the first two equations in (C.1) as

$$\begin{aligned}
&\int_0^L (\mathbf{r}' - \lambda_s\mathbf{t}(\theta))\cdot\tilde{\mathbf{r}}\,ds = 0,\\
&\int_0^L \big[-B(\theta' - \kappa_0)\tilde{\theta}' + \lambda_s\big((\mathbf{t}\times\mathbf{R})\cdot\mathbf{e}_3\big)\tilde{\theta} + m\tilde{\theta}\big]ds = 0.
\end{aligned} \tag{C.4}$$

In addition, we define a secondary domain $\Omega_{2D} = [0, L]\times[-h/2, h/2]$ for the evolution laws of the cis-fraction $n_c(s,z,t)$ and light intensity $J(s,z,t)$, whose weak forms read

$$\begin{aligned}
&\int_{\Omega_{2D}} \Big(\dot{n}_c - \Gamma J(1-n_c) + \frac{1}{\tau}n_c\Big)\tilde{n}_c\,dA = 0,\\
&\int_{\Omega_{2D}} \left(\frac{\partial J}{\partial z} + \mathrm{sgn}(\theta)\frac{1-n_c}{d}J\right)\tilde{J}\,dA = 0,
\end{aligned} \tag{C.5}$$

where $\tilde{n}_c(s,z,t)$ and $\tilde{J}(s,z,t)$ are the associated test fields. We use the `Weak Form PDE` interface to discretize these fields in space by quadratic Lagrange shape functions, and prescribe the Dirichlet boundary condition $J(\theta,z) = \mathrm{sgn}(\theta)\bar{J}\sin(\theta)$ at $z = -\mathrm{sgn}(\theta)h/2$, and zero flux elsewhere. For the time discretization, we choose the Generalized-α method. The coupling between the 1D and the 2D fields is handled using the `general extrusion` and `general projection` operators. In particular, kinematic quantities defined on the 1D domain, such as the local tangent angle, are extruded onto the 2D domain and used to prescribe spatially varying boundary conditions for the light absorption equation. Vice versa, the cis-fraction distribution across the thickness is integrated along z to compute the spontaneous curvature according to Eq. (A.2).

References

Agostinelli, D., DeSimone, A., Noselli, G., 2021a. Nutations in plant shoots: endogenous and exogenous factors in the presence of mechanical deformations. Front. Plant Sci. 12, 371. https://doi.org/10.3389/fpls.2021.608005.

Agostinelli, D., Lucantonio, A., Noselli, G., DeSimone, A., 2020. Nutations in growing plant shoots: the role of elastic deformations due to gravity loading. J. Mech. Phys. Solids 136, 103702. The Davide Bigoni 60th Anniversary Issue. https://doi.org/10.1016/j.jmps.2019.103702.

Agostinelli, D., Noselli, G., DeSimone, A., 2021b. Nutations in growing plant shoots as a morphoelastic flutter instability. Philos. Trans. R. Soc. A: Math. Phys. Eng. Sci. 379 (2201), 20200116. https://doi.org/10.1098/rsta.2020.0116.

Alberts, B., Heald, R., Johnson, A., Morgan, D., Raff, M., Roberts, K., Walter, P., 2022. Molecular Biology of the Cell: Seventh International Student Edition with Registration Card. WW Norton & Company.

Alouges, F., Anello, I., DeSimone, A., Lefebvre-Lepot, A., Levillain, J., 2024. Some mathematical models for flagellar activation mechanisms. to appear on M3AS.

Anello, I., Alouges, F., De Simone, A., 2025. Beating of eukaryotic flagella via Hopf bifurcation of a system of stalled molecular motors. Eur. J. Mech.-A/Solids, 105729.

Bayly, P.V., Wilson, K.S., 2015. Analysis of unstable modes distinguishes mathematical models of flagellar motion. J. R. Soc. Interface 12 (106), 20150124. https://doi.org/10.1098/rsif.2015.0124.

Brokaw, C.J., 1971. Bend propagation by a sliding filament model for flagella. J. Exp. Biol. 55(2). https://doi.org/10.1242/jeb.55.2.289.

Button, B., Cai, L.-H., Ehre, C., Kesimer, M., Hill, D.B., Sheehan, J.K., Boucher, R.C., Rubinstein, M., 2012. A periciliary brush promotes the lung health by separating the mucus layer from airway epithelia. Science 337 (6097), 937–941. https://doi.org/10.1126/science.1223012.

Camalet, S., Jülicher, F., 2000. Generic aspects of axonemal beating. New J. Phys. 2 (1). https://doi.org/10.1088/1367-2630/2/1/324.

Cass, J.F., Bloomfield-Gadêlha, H., 2023. The reaction-diffusion basis of animated patterns in eukaryotic flagella. Nat. Commun. 14 (1). https://doi.org/10.1038/s41467-023-40338-2.

Clarke, B., Hwang, Y., Keaveny, E.E., 2024. Bifurcations and nonlinear dynamics of the follower force model for active filaments. Phys. Rev. Fluids 9. https://doi.org/10.1103/PhysRevFluids.9.073101.

Deng, Z., Zhang, H., Priimagi, A., Zeng, H., 2024. Light-fueled nonreciprocal self-oscillators for fluidic transportation and coupling. Adv. Mater. 36 (12), 2209683.

Gallagher, M.T., Kirkman-Brown, J.C., Smith, D.J., 2023. Axonemal regulation by curvature explains sperm flagellar waveform modulation. PNAS Nexus 2 (3). https://doi.org/10.1093/pnasnexus/pgad072.

Gompper, G., et al., 2020. The 2020 motile active matter roadmap. J. Phys.: Condens. Matter 32 (19), 193001.

Goriely, A., Moulton, D.E., Angela Mihai, L., 2023. A rod theory for liquid crystalline elastomers. J. Elast. 153 (4–5), 509–532.

Gray, J., Hancock, G.J., 1955. The propulsion of sea-urchin spermatozoa. J. Exp. Biol. 32 (4), 802–814.

Howard, J., Chasteen, A., Ouyang, X., Geyer, V.F., Sartori, P., 2022. Predicting the locations of force-generating dyneins in beating cilia and flagella. Front. Cell Dev. Biol. 10. https://doi.org/10.3389/fcell.2022.995847.

Jülicher, F., 1999. Force and motion generation of molecular motors: a generic description. In: Transport and Structure. https://doi.org/10.1007/BFb0104221.

Jülicher, F., Ajdari, A., Prost, J., 1997. Modeling molecular motors. RMP 69 (4). https://doi.org/10.1103/RevModPhys.69.1269.
Jülicher, F., Prost, J., 1995. Cooperative molecular motors. PRL 75 (13). https://doi.org/10.1103/PhysRevLett.75.2618.
Kuznetsov, Y.A., 2023. Elements of Applied Bifurcation Theory. Vol. 112 of Applied Mathematical Sciences. Springer Cham. 4 edition. https://doi.org/10.1007/978-3-031-22007-4.
Lee, E.H., Ouyang, X., Howard, J., 2025. The wavelength of the ciliary beat in chlamydomonas saturates at long ciliary lengths. Biophys. J. 124 (18), 2961–2969.
Lega, J., Goriely, A., 1999. Pulses, fronts and oscillations of an elastic rod 132 (3), 373–391. https://doi.org/10.1016/S0167-2789(99)00047-0.
Lindemann, C.B., 1994. A model of flagellar and ciliary functioning which uses the forces transverse to the axoneme as the regulator of dynein activation. Cell Motil. Cytoskeleton 29 (2). https://doi.org/10.1002/cm.970290206.
Machin, K.E., 1958. Wave propagation along flagella. J. Exp. Biol. 35 (4), 796–806.
Meirovitch, L., 1997. Principles and Techniques of Vibrations. Prentice Hall, Upper Saddle River, NJ.
Moulton, D.E., Oliveri, H., Goriely, A., 2020. Multiscale integration of environmental stimuli in plant tropism produces complex behaviors. Proc. Natl. Acad. Sci. 117 (51), 32226–32237.
Namdeo, S., Onck, P.R., 2016. Emergence of flagellar beating from the collective behavior of individual ATP-powered dyneins. Phys. Rev. E 94 (4), 042406.
Norouzikudiani, R., Lucantonio, A., DeSimone, A., 2023. Equilibrium and transient response of photo-actuated liquid crystal elastomer beams. Mech. Res. Commun. 131, 104126.
Norouzikudiani, R., Teresi, L., DeSimone, A., 2024. Self-oscillations of submerged liquid crystal elastomer beams driven by light and self-shadowing. J. Elast. 156 (4), 1243–1260.
Oriola, D., Gadêlha, H., Casademunt, J., 2017. Nonlinear amplitude dynamics in flagellar beating. R. Soc. Open Sci. 4 (3). https://doi.org/10.1098/rsos.160698.
Riedel-Kruse, I.H., Hilfinger, A., Howard, J., Jülicher, F., 2007. How molecular motors shape the flagellar beat. HFSP J. 1 (3). https://doi.org/10.2976/1.2773861.
Sartori, P., Geyer, V.F., Scholich, A., Jülicher, F., Howard, J., 2016. Dynamic curvature regulation accounts for the symmetric and asymmetric beats of Chlamydomonas flagella. Elife 5. https://doi.org/10.7554/eLife.13258.
Satir, P., Christensen, S.T., 2007. Overview of structure and function of mammalian cilia. Annu. Rev. Physiol. 69 (1), 377–400. https://doi.org/10.1146/annurev.physiol.69.040705.141236.
White, T.J., Tabiryan, N.V., Serak, S.V., Hrozhyk, U.A., Tondiglia, V.P., Koerner, H., Vaia, R.A., Bunning, T.J., 2008. A high frequency photodriven polymer oscillator. Soft Matter 4 (9), 1796–1798.
Wiggins, S., 2003. Introduction to Applied Nonlinear Dynamical Systems and Chaos. Texts in Applied Mathematics, Springer.
Woodhams, L.G., 2025. Ciliary wavelength has its limits. Biophys. J. 124 (18), 2929–2930.
Zeng, H., Lahikainen, M., Liu, L., Ahmed, Z., Wani, O.M., Wang, M., Yang, H., Priimagi, A., 2019. Light-fuelled freestyle self-oscillators. Nat. Commun. 10 (1), 5057.